

Spectroscopic study of neutron-capture elements in CEMP and Barium Stars



Thesis submitted to
Indian Institute of Science Education and Research, Pune
in partial fulfillment of the requirements for the
BS-MS Dual Degree Programme

by

Rajeev Singh Rathour

under the guidance of

Dr Aruna Goswami

Associate Professor,
Indian Institute of Astrophysics

INDIAN INSTITUTE OF SCIENCE EDUCATION AND RESEARCH
PUNE

© All rights reserved

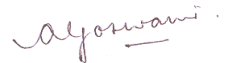
**Dedicated to Prof. Richard P. Feynman
and Prof. Margaret Burbidge.**

Certificate

This is to certify that this dissertation entitled **Spectroscopic study of neutron-capture elements in CEMP and Barium Stars** submitted towards the partial fulfilment of the BS-MS dual degree programme at the Indian Institute of Science Education and Research, Pune represents original research carried out by **Rajeev Singh Rathour** at the **Indian Institute of Astrophysics**, Bangalore, under the supervision of **Dr. Aruna Goswami** during the academic year **2017-2018**.



Student
Rajeev Singh Rathour



Supervisor
Dr. Aruna Goswami

Date: 20/3/2018

Declaration

I hereby declare that the matter embodied in the report entitled **Spectroscopic study of neutron-capture elements in CEMP and Barium Stars** are the results of the investigations carried out by me at the Department of Stellar Physics, Indian Institute of Astrophysics, Bangalore under the supervision of **Dr Aruna Goswami** and the same has not been submitted elsewhere for any other degree.



Rajeev Singh Rathour

Date: 20/3/2018

Acknowledgements

I would like to thank my supervisor Dr Aruna Goswami (IIA, Bangalore) for introducing me to the field of Stellar Astrophysics and for being kind to me in the learning process. I would like to thank the PhD students of my research group for teaching me the reduction and analysis techniques in the beginning phases. I would like to thank Soumya and Partha for their helpful physics discussion. I also thank the people in IAO and CREST who have helped and supported me with their assistance during the observations.

I am grateful to Dr Prasad Subramanian for being my mentor in IISER for more than two years now and providing me all kinds of support. Special mention to IISER education system for giving me this opportunity to take up a thesis project outside my institute and laying down the foundation for my Astronomy career. Most importantly, a big thanks to the scientific community for their immense contribution to the literature and the field as well. Also, I would like to thank the three gems of my IISER life, Shruti, Saurabh and Swanand for being the anchor to my chaotic life and providing local meaning to my life with intellectual solace. This work is partly dedicated to them. Last but not the least, to my brother Sanju and my dad, without whom, I would not have been where I am right now.

Abstract

In the quest for understanding the early universe we have come to a line of thought of looking for Metal-poor stars since they carry the fingerprint of the very first stars formed. The study of the elements produced or preserved in these stars gives a fundamental insight into the chemical evolution on a much larger scale. To understand the composition of such stars and their distribution in the galaxy, there exists a need for High-resolution spectroscopic studies on target stars which show neutron-capture elements enhancement. Therefore, in this work we present the detailed chemical abundance analysis of objects HD 179832, HD 145777 and HE 2144-1832 using High-resolution spectra of facilities such as FEROS (Fibre-fed Extended Range Optical Spectrograph) and HESP (High Resolution Echelle Spectrograph). We do a series of reductions procedures using IRAF to obtain final spectra, followed by metallicity estimate and determining model atmosphere parameters such as effective temperature, surface gravity and micro-turbulent velocity of the programme stars. Then we use these to do chemical analysis of species such as α -elements, Fe-peak elements and neutron-capture process elements using the latest version of spectral analysis code MOOG. We present the mass and age of the stars determined using the up to date models of stellar evolutionary track and isochrones.

The object HD 179832, HD 145777 and HE 2144-1832 have $[\text{Fe}/\text{H}]$ 0.22, -2.14 and -1.60 respectively. These are classified as Barium star, CEMP-s star and CEMP-r/s star respectively by our analysis. We also report analysis of more than 15 elements including α elements such as Mg, Ca, Ti; Iron-peak elements such as Co, Ni, and Zn; light neutron-capture elements like Sr, Y and heavy neutron-capture elements Ba, La, Nd, Sm, Eu.

At the end of the report we attempt to classify our results with respect to the large sample of existing literature on the concerned system. Using Kinematic analysis and nucleosynthesis theories we present some conclusions on galactic distribution of these stars and origin of the elements produced by them.

Contents

1	Introduction	6
1.1	Stellar Evolution	7
1.2	Neutron-capture Nucleosynthesis	11
2	Theory	13
2.1	Background	13
2.2	CEMP and Barium Stars	14
2.2.1	Carbon Enhanced Metal-poor stars	14
2.2.2	Barium stars	16
2.3	Aims and objectives	17
3	Spectroscopic Methodology	18
3.1	Observations	18
3.2	Data Reduction	19
3.2.1	IRAF	19
3.3	Data Analysis	23
3.3.1	Radial Velocity Measurement	23
3.3.2	Kurucz Model Atmosphere	24
3.3.3	MOOG	25
3.3.4	Line analysis	26
4	Results and Discussion	29
4.1	Basic star data	29
4.2	Photometric Temperature Estimates	31
4.3	Atmospheric parameters	32
4.4	Chemical abundances	33
4.4.1	HD 179832	36
4.4.2	HD 145777	37
4.4.3	HE 2144-1832	38
4.5	Mass and age determination	41
4.6	Kinematic analysis	44

4.7	Error Analysis	46
4.8	Comparative studies	47
4.8.1	Atmospheric Parameters	47
4.8.2	Kinematics	49
4.8.3	Chemical Abundances	50
5	Conclusions	60
5.1	Existing Nucleosynthesis Theory	60
5.2	Object-wise conclusions	61
5.2.1	HD 179832	61
5.2.2	HD 145777	63
5.2.3	HE 2144-1832	64
	References	65
A		71
A.1	Python Codes	71
A.1.1	Photometric Estimate	71
A.1.2	Kinematic Analysis	72
A.2	Line-lists	74

List of Tables

2.1	Subclasses of Neutron capture rich metal poor stars. Reference: Beers et al 2005	15
2.2	Subclasses of Carbon-enhanced metal poor stars. Reference: Beers et al 2005	15
4.1	Basic data for the program stars. Source: Simbad Database	29
4.2	Fluxes in different bands. Source: Simbad Database	30
4.3	Radial velocities V_r of the programme stars	30
4.4	Photometric estimates of programme stars for $[\text{Fe}/\text{H}] \leq 0$	31
4.5	Photometric estimates of programme stars for $[\text{Fe}/\text{H}] \leq -1$	31
4.6	Photometric estimates of programme stars for $[\text{Fe}/\text{H}] \leq -2$	31
4.7	Spectroscopic Atmospheric parameters results	32
4.8	Light elements abundances $[\text{X}/\text{Fe}]$ and C/O ratio	35
4.9	Equivalent width and spectrum synthesis analysis results: HD 179832	36
4.10	Equivalent width and spectrum synthesis analysis results: HD 145777	37
4.11	Equivalent width and spectrum synthesis analysis results: HE 2144-1832	38
4.12	Distance, Bolometric correction, Extinction coefficient and Bolometric magnitude of the programme stars	41
4.13	Calculations from Parallax	43
4.14	Kinematic analysis results	45
4.15	Velocity dispersions, asymmetric drift velocities, and the fractional population of three stellar components.	45
4.16	Galactic Distribution Probability results	46
4.17	Abundance ratios	58
A.1	Element Line-list HD 179832	74
A.2	Fe Line-list HD 179832 continuing	75
A.3	Element Line-list HD 179832	76
A.4	Element Line-list HD 179832 continuing	77

A.5	Element Line-list HD 179832 continuing	78
A.6	Fe Line-list HD 145777	79
A.7	Element Line-list HD 145777	80
A.8	Element Line-list HD 145777 continuing	81
A.9	Line-list of HE 2144-1832	82
A.10	Element Line-list HE 2144-1832	83
A.11	Element Line-list HE 2144-1832 continuing	84

Chapter 1

Introduction

Spectroscopy has been one of the tremendous tool to study the optical region since the past. Similarly the ingenious idea of astronomical spectroscopy as a techniques to measure electromagnetic radiation, in the visible region, which radiates from stars and other celestial objects reveals some of the fundamental properties of a star like its temperature, velocity and chemical composition. Along with this, a further extension can very well be used to infer mass and distance of the object. Spectroscopy is not limited to only visible region but spans from radio waves to gamma rays. By the end of this manuscript we will use optical spectroscopy to estimate these properties and finally put into perspective some of the fundamental features the nature demonstrates.

Spectroscopy can be done at two resolutions:

- Low-Resolution Spectroscopy helps in classification of stars by identification of various bands, for example: C₂,CN,CH band, etc.
- High-Resolution Spectroscopy gives more resolved lines for identification and measurement to derive chemical elemental abundances.

Hence, we have undertaken a High-Resolution Spectroscopic study of objects HD 179832, HD 145777 and HE 2144-1832 to determine some major aspects of stellar properties in context to the galactic chemical evolution.

1.1 Stellar Evolution

Stars, just like humans are born, go through evolutionary phases, age and then ultimately die. This just happens on a much larger time-scales, usually a few million to billion years depending on the initial mass. We will restrict our case to only low ($0.8M_{\odot} - 2.25M_{\odot}$) and intermediate ($2.25M_{\odot} - 8M_{\odot}$) mass stars. These divisions are on basis of minimum criteria for certain core burning phases. The $0.8M_{\odot}$ division is for the minimum mass required to go through central Helium burning phases [42]. The core helium burning phase converts from degenerate and non-degenerate case at around $2.25M_{\odot}$. And finally core carbon burning does not occur below $8M_{\odot}$, which distinguishes between intermediate mass stars and high mass stars. Another division exists between low mass stars and intermediate mass stars on the basis of Hot bottom burning (HBB) process at $4M_{\odot}$. We will talk about this process in the later chapters.

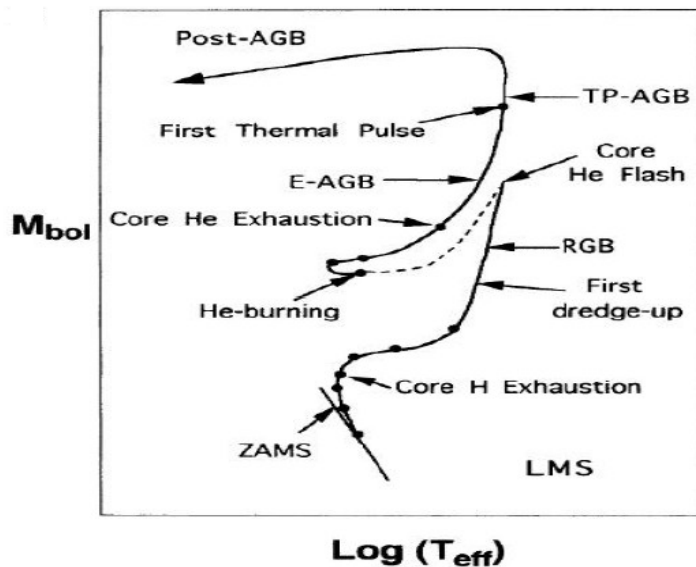


Figure 1.1: Stellar evolution of $1M_{\odot}$ star.

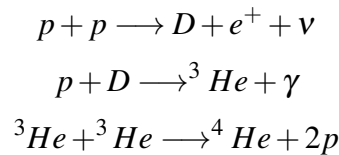
Image Reference: http://www.mso.anu.edu.au/~akarakas/Kodai_Lecture1.pdf

Pre-main sequence The universe consists of Interstellar matter (ISM) which is the birthplace of a star. The initial process is not very well understood but its very much established that the gas clouds due to certain instabilities or density fluctuations in by nearby environments cause it to collapse under its own gravity. As the process goes on, more and more gas and material is dumped onto the centre,

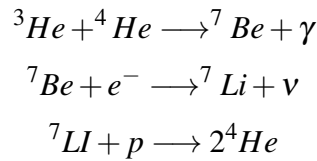
leading to a temperature rise during the collapse. At this point it still remains a dense cloud and not a star.

Main Sequence After the previous mentioned scenario as it attains a certain temperature $\sim 10^7 K$, the core is now ready to burn Hydrogen to produce Helium. Such a point is a distinction of a star from a cloud and hence the longest phase of a star's life called Main sequence begins. Since there is no reason why gravitational infall of matter should stop, so to balance the gravity, there are nuclear fusion reactions releasing immense energy as radiation pressure. This process of conversion of Hydrogen to Helium is done via different chemical reactions occurring at the centre of the star simultaneously. One such type is proton-proton chain reactions.

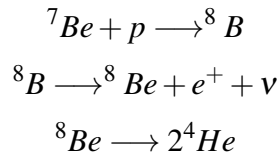
PP I chain:



PP II chain:

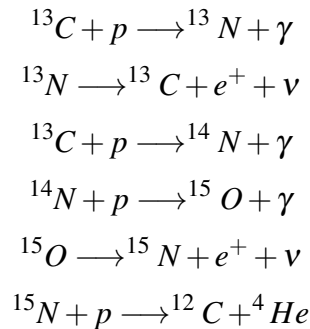


PP III chain:

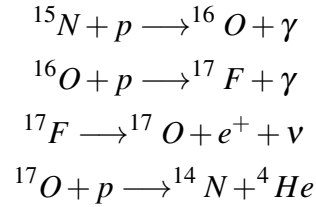


At a temperature higher than $\sim 2 \times 10^7$, CNO cycle dominates in producing He and energy to balance the gravitational force.

CN cycle:



NO cycle:



Red giant phase (RGB) When most of the Hydrogen is burnt into Helium, the process ceases for a while. The product of the reaction is dumped on to the core surrounded by a Hydrogen burning shell. Now there are two scenarios that can occur from here. In low mass stars the Helium core contracts enough so as to attain a degenerate state. So now the degeneracy pressure balances the gravity infall of the outer layers. The important point to make here is that this degeneracy pressure is dependent on density and not temperature, which is unlike the thermal pressure. In intermediate mass stars, the mass of the core is just enough to contract and ignite some Helium burning to support the infall. This produces elements such as Carbon and oxygen.

Consequently, as the core contracts, the outer layer of the star expands and cools down attaining lower temperature. This temperature corresponds to higher wavelength and the star appears redder in colour along its evolutionary path and hence the name Red Giant Branch. As the star evolves further and expands, it can reach up to a few hundred sun's radius. In such conditions the temperature falls down and luminosity increases so it becomes quite clear why it moves up the HR diagram almost vertically. Luminosity is given by the relation:

$$L = 4\pi\sigma R^2 T^4 \quad (1.1)$$

By this time the envelope is deep enough to become convective and triggers the convective belts to give onset to an event called the 'First dredge-up' which changes the surface composition of the star. The abundance of ${}^4\text{He}$ and ${}^{14}\text{N}$ increases whereas Carbon decreases. As the core heats up further, the triple α process kicks in which has a very steep dependence on temperature. Also the core of the star at this point lacks any thermostatic control so now as the temperature increase, there is no increase in the pressure. Hence this results in a violent flash triggering Helium burning known as 'Helium flash'. This happens at the tip of the RGB and marks the end of this evolutionary phase.

Horizontal giant branch (HB) The Helium flash provides the sudden thermonuclear kick to the core and hence the core is now busy converting Helium to other elements which it deposits at the core. A single Helium flash can produce luminosities of the order of $10^9 L_{\odot}$ which is around the luminosity of a local

galaxy. The star encounters an increase in temperature and moves horizontally along the HR diagram. The core mostly depleting its Helium burning resources marks the end of this phase.

Asymptotic giant branch (AGB) The most important in terms of stellar nucleosynthesis is the the Asymptotic giant branch (AGB) phase. It is characterised by its double shell (Helium and Hydrogen) burning on either sides of the Helium intershell region. The outermost part is the Convective envelop and the innermost part is a dormant CO core. A star usually spends one tenth of its main sequence lifetime in this phase producing the most heavy elements which further enriches the universe. The second dredge up occurs at this phase only in intermediate stars as the H shell burning is active in low mass stars, which prevents the convective envelop from penetrating. There are two major parts of this phase, Early AGB phase and the Thermally pulsating AGB (TP-AGB) phase. We will discuss more on the nucleosynthesis happening in these phases in the next [section 1.2](#).

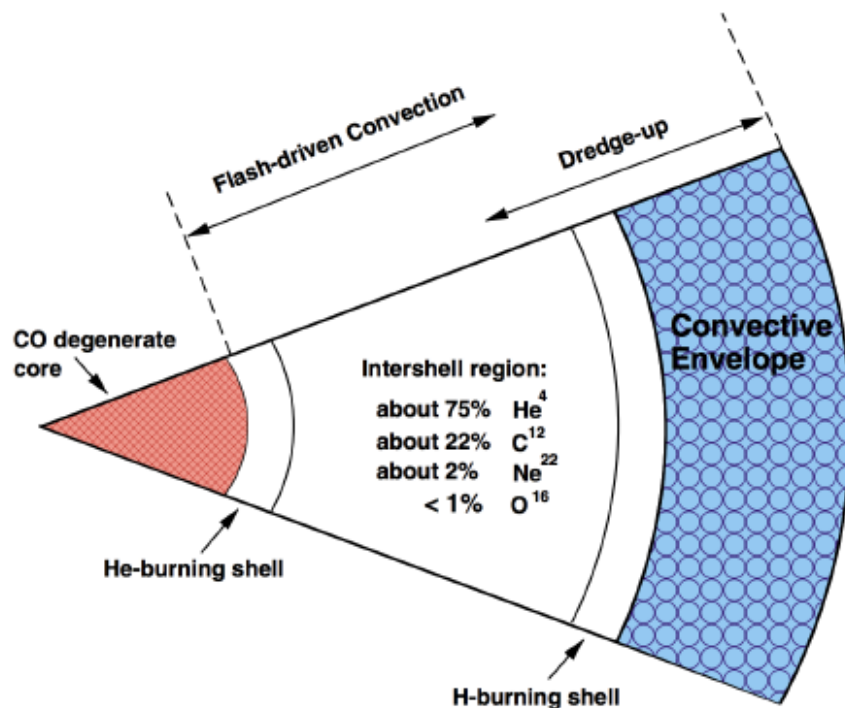


Figure 1.2: A schematic representation of AGB double shell. (Karakas2010)

Planetary Nebula As the stellar envelop expands further, there comes a point when a significant mass fraction falls outside the gravitational potential of the star. In such cases the envelop no longer belongs to the star. The strong winds produced by radiation pressure coming from the deeper layers of the star pushes this envelope far outside leaving behind a dormant CO core referred to as white dwarf.

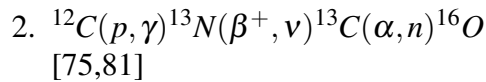
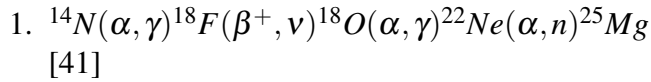
1.2 Neutron-capture Nucleosynthesis

Stellar interior is the place for forming various elements via fusion reactions occurring at a very high temperature. However, there is limit to how much fusion can contribute to the periodic table elements we see today. Due to the saturation of the Nuclear binding energy per nucleon at Iron, fusion cannot produce elements heavier than Fe. Even more interesting process known as fusion takes over here and produces heavier elements by processes such as neutron/proton capture and beta/gamma decays. It requires temperature along with high neutron flux. The so called seed nuclei such as those of Iron or Nickel act as a target which are bombarded by high neutron flux which is called as neutron irradiation. These Fe seed nuclei captures a neutron and then beta-decay to form heavier elements and hence the nucleosynthesis of heavy elements takes place. Depending upon the competition between rates of neutron capture and beta-decay, these are classified as r-process (rapid) and s-process (slow). Barium is the key element for the indication of s-process efficiency where Europium represents the same for r-process. We will discuss their implication on production of other elements in later sections along with observational data.

The AGB phase is important in stellar evolution as it is the richest phase in terms of nucleosynthesis. But on the other hand it is hard to model completely because it constitutes of only 1 percent of the star's whole lifetime. Also the circumstellar dust surrounding the star this point cause an observational constraint in the optical region. Low mass ($0.8M_{\odot} - 2.5M_{\odot}$) AGB stars have longer Main sequence life as well as total stellar lifetime than intermediate and massive stars by few orders of magnitude. Therefore, these low mass AGB stars enrich the universe on a much slower rate (50 Myr to few Gyr) as compared to supernova which are short-lived. Therefore using observational constraints and existing nucleosynthesis physics, it becomes very important to model these right from their formation to main sequence to AGB phase to final surface abundances. Our discussion will mainly be centred in and around AGB phase.

Nucleosynthesis in AGB Asymptotic giant branch phase is the most natural niche for nucleosynthesis of heavier elements simply because of the presence of free neutrons at optimum densities and the required temperature.

Two reactions which are the major neutron sources in AGB stars:



These two above reactions govern the major dynamics of what element is to be produced in what proportion. In low mass star almost all of the neutron exposure is provided by radiative burning of ${}^{13}\text{C}(\alpha, n){}^{16}\text{O}$ reaction. This occurs at temperature around $9 \times 10^7 \text{K}$ during the interpulse period of the Thermally Pulsating AGB phase. ${}^{22}\text{Ne}(\alpha, n){}^{25}\text{Mg}$ reaction contributes very less as it requires higher temperature. This temperature is achieved by intermediate mass stars and thus the ${}^{22}\text{Ne}(\alpha, n){}^{25}\text{Mg}$ reaction forms the major part of the nucleosynthesis stage provided. This reaction operates at temperatures around $3.5 \times 10^8 \text{K}$ which is attained during the thermal pulses. [93]

Chapter 2

Theory

2.1 Background

The unclear picture of the origin and evolution of neutron-capture elements in our Galaxy still exists. That is why CH stars, their metal poor counterpart Carbon-enhanced metal-poor (CEMP) stars along with barium stars have been studied from a very long time for decades since they synthesize and preserve these neutron-capture elements within them. These class of stars help us to uncover the processes by which they produce the elements along with what their distribution is in the environment. These are one of the best probes to study the early universe as they carry the chemical signatures of the very first stars i.e. population III stars. The term metal-poor or metal-rich is coined with respect to the solar abundances of the corresponding elements. The abundances are calculated as a solar scaled log value given by the following relation:

$$\left[\frac{A}{B}\right] \equiv \log_{10}\left(\frac{N_A}{N_B}\right)_* - \log_{10}\left(\frac{N_A}{N_B}\right)_{\odot} \quad (2.1)$$

Where N_A and N_B are number densities of respective elements. The second term on the right is to scale these number densities ratio to solar values on a logarithmic scale. There exists absolute abundance formula which is calculated with respect to number density of Hydrogen atoms given by:

$$\log\mathcal{E}(A) \equiv \log_{10}\left(\frac{N_A}{N_B}\right) + 12.0 \quad (2.2)$$

2.2 CEMP and Barium Stars

Barium stars and Carbon Enhanced Metal-poor (CEMP) stars have a common feature which is the presence of signatures of neutron-capture elements in their spectra. However they do differ on a few grounds such as metallicity ranges, kinematic distribution and Carbon enhancements. We will introduce both these classes and discuss on the above mentioned aspects here in this section.

2.2.1 Carbon Enhanced Metal-poor stars

From a long time CH star have been classified on a basis of its two key features; strong G band of CH along with enhancement shown in neutron-capture elements. These population II stars are further divided to two subclasses depending upon the Carbon isotopic ratio ($^{12}\text{C}/^{13}\text{C}$). These stars are also characterized by high spatial velocity. Carbon Enhanced Metal-poor stars are the metal-poor counterpart of CH star class. CEMP are an important stellar sites to probe into the origin of pristine elements and develop a consistent model of galactic chemical evolution. These are the prime targets as their population fraction increases as we dig into more and more metal-poor stars [74]. There are different categories of star on the basis of how less their abundances are with respect to solar. This is clear from the Table 2.1 and Table 2.2. Previous surveys [30] have suggested that these stars are as metal poor as $[\text{Fe}/\text{H}]=5.4 \pm 0.2$ which accounts to abundance around 10^{-5} lesser than the solar value. CEMP stars show enhancement of neutron-capture elements which has quite a big scatter in the found metallicity ranges. Therefore these stars have further classification on the basis of the enrichment of these elements and Carbon content (See Table 2.1 and Table 2.2).

Stars with Barium enhancement are called s-process enhanced stars whereas stars with Europium enhancement are called r-process enhanced stars mainly because they represent the s-process and r-process peak respectively in the abundance v/s atomic number plot. The s and r depicts the competition of rate of neutron capture by the seed nuclei against the beta decay rate, during the nucleosynthesis of these elements [24]. The s stands for slow whereas the r stands for rapid. There also exists a proton enriched p-process but that is beyond the scope of this study. Most of the lower atomic number elements constitutes these s-process elements whereas the higher Z elements constitute the r-process ones. The s-process has further division of light s-process elements such as Sr, Y, and Zr with atomic numbers $Z = 38, 39,$ and $40,$ respectively and heavy s-process elements such as Ba, La, Ce with atomic numbers $Z = 56, 57,$ and $58,$ respectively.

The solar abundances with which definitions of stars are scaled are the estimates from either solar photosphere or meteorite studies conducted. Our study

Table 2.1: Subclasses of Neutron capture rich metal poor stars.
Reference: [Beers et al 2005](#)

r -I	$0.3 \leq [\text{Eu}/\text{Fe}] \leq 1.0$	$[\text{Ba}/\text{Eu}] < 0$
r -II	$[\text{Eu}/\text{Fe}] > 1.0$	$[\text{Ba}/\text{Eu}] < 0$
s	$[\text{Ba}/\text{Fe}] > 1.0$	$[\text{Ba}/\text{Eu}] > 0.5$
r/s		$0.0 < [\text{Ba}/\text{Eu}] < 0.5$

Table 2.2: Subclasses of Carbon-enhanced metal poor stars.
Reference: [Beers et al 2005](#)

CEMP	$[\text{C}/\text{Fe}] > 1.0$		
CEMP-r	$[\text{C}/\text{Fe}] > 1.0$	$[\text{Eu}/\text{Fe}] > 1.0$	
CEMP-s	$[\text{C}/\text{Fe}] > 1.0$	$[\text{Ba}/\text{Fe}] > 1.0$	$[\text{Ba}/\text{Eu}] > 0.5$
CEMP-r/s	$[\text{C}/\text{Fe}] > 1.0$		$0.0 < [\text{Ba}/\text{Eu}] < 0.5$
CEMP-no	$[\text{C}/\text{Fe}] > 1.0$	$[\text{Ba}/\text{Fe}] < 1.0$	

uses the updated solar values [9]. C/O ratio in CH stars is observed in various studies to be greater than unity [86, 69]. This definition of ratio [88] is an important characteristic which separates it from Barium star class of objects.

There have been proposed different scenarios considered for enrichment of CEMP-s and CEMP-r/s stars. For s-process enrichment binary AGB nucleosynthesis model is considered where the star we observe (secondary) is in a binary configuration with an evolved star (primary). This primary star completes the AGB phase and becomes a white dwarf and in the process expels out s-process enriched matter which is then accreted by the secondary star that we observe, via two major mechanisms i.e. Roche lobe overflow (RLOF) and wind-accretion. Most of the CEMP-s stars have found to be in a binary system as per several long term radial velocities monitoring. This class of stars covers as much as 80 percent of the total CEMP sample available [3]. Apart from this nucleosynthesis happening in the inter-shell region of the secondary star again contributes to the both light and heavy s-process enrichment. This material is brought to the surface via different processes like convective mixing (due to temperature gradient), non convective processes like thermohaline mixing (due to density gradient), rotation mechanism and Third dredge up.

On the other hand r-process enrichment too have different proposed models such as the primary not being a AGB star but a type 1.5 supernova [92, 89] or the star falling on the other via an accretion-induced collapse [71, 25] or a theoretically rare scenario of a triple star system having a massive star responsible for enriching the secondary star [25] or at last a primordial origin, so as to say the environment in which the birth of our binary took place was already polluted

by r-process elements [17]. There is also a CEMP-no star class where carbon is enhanced with not the neutron-capture elements. These stars mostly have their niche in outer halo of the galaxy [22] whereas what is interesting about this class in particular is their frequency at extremely low metallicity ($[Fe/H] < -3$) as shown by Aoki et al. [3].

2.2.2 Barium stars

Barium stars are basically a class of stars, of spectral type G and K, in redgiant phase showing a strong Ba II line at 4554 Å along with over-abundance in s-process elements which are produced by neutron-capture processes. These also show carbon enhancements ($0.4 < [C/Fe] < 1.2$ [7, 4, 29, 69]) and bands such as CH, CN, and weak C_2 in their spectra. These were very first identified by Keenan's 1951 paper [16]. There is further subdivision on the basis of strength of this 4554 Å Ba II line, mainly Strong Ba stars ($Ba=2.5$) and mild Ba stars ($Ba < 2$). The more tighter definition is the Barium abundance $[Ba/Fe]$. Under this classification strong Ba stars has $[Ba/Fe] > 0.6$ and the rest below belongs to mild ones [87]

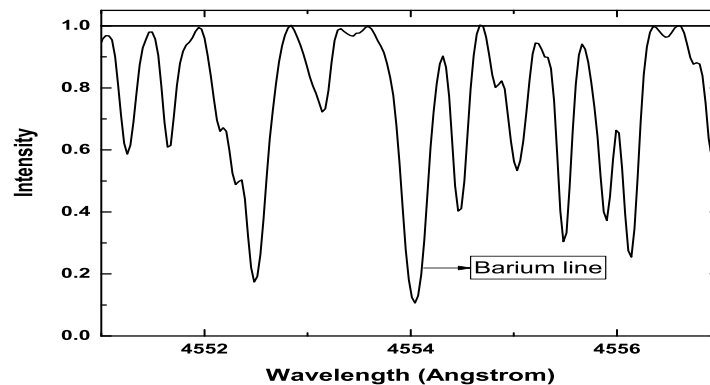


Figure 2.1: Strong Ba II line at 4554 Å in our spectra of HD 179832

Barium stars have a common property of belonging to either thin or thick disk populations in the galaxy. Studies [65] have looked into the kinematics of this class to confirm this feature of being disk objects. Other than this feature, as mentioned in the previous section, Barium stars also have C/O ratio less than unity [10, 4, 29, 69].

Now we come to the neutron-capture elements observed in Barium stars. Earlier studies [42] have revealed the knowledge that mostly stars with luminosities in the range $-5 < M_v < -3$ which go through Thermally pulsating AGB (TP-AGB) phase show s-process enhancements, via an event called "third dredge-up". This led to the puzzle of where these enrichment might come from since Barium stars belong to redgiant phase. Later works [63, 64, 45] showed with their long term radial velocity monitoring studies that Ba stars belong to a binary system with a non-visual companion. This scenario was similar to the CEMP stars as discussed in subsection 2.2.1 therefore is attributed to the similar binary AGB picture. Barium stars are mostly found as metal-rich or with near solar metallicities and sometimes moderately metal-poor. Due to this nature they are referred to be analogous to Cemp-s stars, in the sense that they represent the metal-rich population I part of CEMP-s stars. This has further given hints to the researchers towards their common ancestry.

2.3 Aims and objectives

1. Methodology of spectroscopic data analysis:
 - Line identification.
 - Equivalent width measurement.
 - Determination of stellar atmospheric parameters using equivalent widths and model atmosphere.
 - Estimation of elemental abundances.
2. Interpretation of results
 - Estimates of Abundance ratios with respect to metallicity.
 - Mass and Age determination.
 - Kinematic analysis.
 - Comparative analysis with literature data.

Chapter 3

Spectroscopic Methodology

3.1 Observations

In this work we present the detailed chemical abundance analysis in context to stellar nucleosynthesis studies of objects HD 179832, HD 145777 and HE 2144-1832. These programme stars are taken from the CH star catalogue of Bartkevicius [12]. HD 145777 and HE 2144-1832 are observed with HESP (High Resolution Echelle Spectrograph) facility of Himalayan Chandra Telescope (HCT), Hanle . The instrument has resolution of $R \sim 60,000$ and covers the spectral range of 3,500-10,000 Å. We have also worked upon a FEROS (Fibre-fed Extended Range Optical Spectrograph) spectrum of HD 179832. This spectrograph with resolution of $R \sim 48,000$ is on-board 1.52m ESO telescope at Chile. The wavelength coverage is 3,500-9,000 Å.

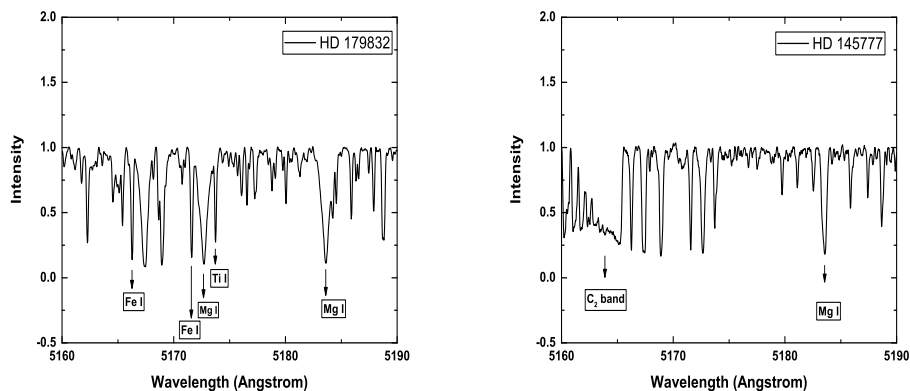


Figure 3.1: Sample spectra of the program stars (5160-5190Å)

The major HESP facility that we have used in this project has a set-up which gives a 4K x 4K CCD detector with pixel size of 15μ and wide coverage of 350 – 1000 nm at a spectral resolution of $R \sim 30,000$ and 60,000. This means it could be used at medium as well as high resolution mode. The advantage about this new facility is that it provides this spectral coverage in one instrumental set-up at a time. This avoids any kind of calibration error and wavelength break in the spectrum.

3.2 Data Reduction

This section covers the details about IRAF spectroscopic reductions and abundance analysis methods used in this work.

3.2.1 IRAF

The flowchart of the reduction procedure is given in the Figure 3.2. We will go over each part of it in the discussion below.

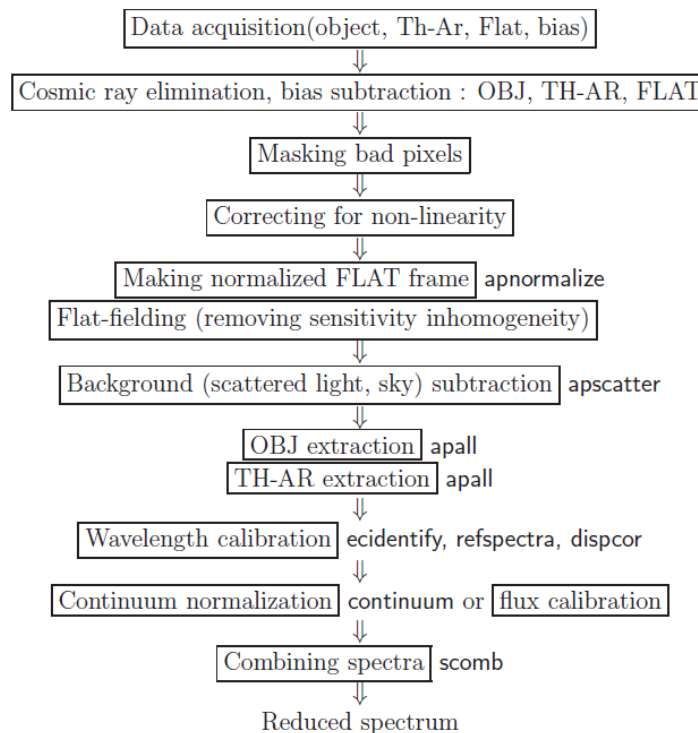


Figure 3.2: References: Reduction Manual, Wako Aoki, Krzysztof Hełminiak National Astronomical Observatory of Japan

Subtraction of the over-scan The CCD (Charge Coupled Device) has different units that receive signal. The scan of the CCD is not done end to end but a little further so as to not miss any photon count. In doing this, we get over-scan regions where there is no CCD but gives false zero counts. These are removed by taking average counts from each over-scan unit and dividing it later by the corresponding unit. These regions of over-scan as well as the average CCD counts can be checked by using DS9 software which displays the CCD counts from the fits file. Alternative way is to use DISPLAY command and identify the bad regions.

Trimming This task gives the input of the trim section of the CCD scan so as to exclude the regions not needed for spectra extraction. Usually its well defined for the instrument and the trimsection we use is [50:4137,300:3600] on a pixel X pixel scale horizontally and vertically. First we create a trimfile and copy it to trimoutput, then use this as input and output parameter respectively in the CCDPROC task.

Object/Star Combine We usually take 3 frames for each object/star to be observed and then average it to compensate for the low counts (if any) in the given spectral range. All 3 frames are for exactly the same wavelength coverage. We use the task IMCOMBINE to combine these object frames. The input is all 3 frames and the output is an averaged combined file.

Bias Combine The very important task is to remove any bias in the data file after the observation. The bias files (typically 3 frames) contains the CCD readout when the aperture is close or completely covered. This is done so as to remove the zero counts or dark current received by the CCD due to cosmic rays which penetrate into the instrument during the observation. These counts create strong intensity lines in the data which are not from the object/star. So we combine these 3 frames of bias files by using the task ZEROCOMBINE to create a masterbias fits file which can be used in the later section for bias subtraction. The input for the task is all 3 frames and the output is materbias.fits.

Bias Subtraction Following the previous task, now we need to remove this bias from the object/star files. We use task CCDPROC With input object fits file, output bias corrected object fits file, and reference as masterbias. Hence the cosmic ray corrections are taken into account

Flat normalisation There are series of CCDs on the detector which may not have the same response to the incoming flux of light/signal. By this we mean that if pixel 1 generates a photo current on 2 counts of detection, the pixel 2 can

respond the same in 1 count of detection and so on. At high electron numbers the CCD is slightly less sensitive than at low. Up to some limit the response is said to be linear (for electron numbers $< 10,000e^-$ ($\sim 6,000$ ADU) while the non-linearity is declared at $50,000e^-$. Flat comes into picture as the remedy to normalise this response variation. Flat is obtained by checking CCD response to a constant intensity light for a long time span. So we need to take into account this effect and normalize this response of the CCD at all the segments. We do this by using task FLATCOMBINE and put parameters input as all the flat frames (typically 5), output as masterflat.fits file and combine as average. After we combine all the flats to obtain masterflat, using task APFLATTEN we can do flat normalisation on the object/star scans. Put input as masterflat and output as nmasterflat (normalised masterflat). Now this output file can be applied to the object/star.

One important thing to note is that this task of flat field correction is not always to be applied to the data. In our reduction the flat field introduced some extra unwelcomed features into the spectra so we did not use flat correction to our data. This implies that the response of the HESP detector is near perfect as there is no change in the response along the CCD.

Aperture Tracing In this procedure we mark the apertures one by one identifying the signal region to the left and right of the corresponding apertures. The shapes of the apertures and zoom in view of a single aperture is shown below. Keys N, L and U are used to fix the middle, left and right part of the aperture respectively. In high resolution case there will be around 50-60 apertures to mark. It is important to mark these apertures carefully, without missing any as these markings as these will be later applied to the other files taking this as reference.

Dispersion axis check This step is very important so as to check the dispersion axis of the spectra, being either horizontal or vertical. For this we have to go out of the echelle package and use twodspec package. Then in the task ECHELLE check parameter dispaxi. This is set to 1 (Horizontal) in high resolution spectra and 2 (vertical) in low resolution spectra. Since we are reducing high resolution data here, we set it to 1.

Extraction of Spectra The next step is to extract the spectra from the given marked aperture files. This spectra is initially intensity v/s pixel on the CCD which will later after calibration be converted to the required intensity v/s wavelength form. However the major lines can be easily identified even in this form.

Background Subtraction/Scatter Correction There is always some residual counts in the region between adjacent orders of the spectra which needs to be

removed from the aperture plots. The cause of this extra feature is the scattered light inside spectrograph. The idea to remove this is to use task APSCATTER to mask the apertures and then do a surface fit to the background region. This step is done only to objects/stars and the reference parameter is set to the object frame for which the order trace and extraction is once made. After executing the task, appropriate function (spline1, spline3, legendre, chebysev) and order (1 to 30) is chosen to do the fit.

Wavelength Calibration This is the most time consuming and important task of all where we use the high resolution Th-Ar ATLAS (wavelength range 3,650 Å-10,550 Å) intensity lines of the already marked apertures and use them to apply to our Th-Ar extracted spectra files. A one to one matching of the aperture between the Th-Ar and the observed spectra is done. A point to note that the intensity of lines may vary amongst the given spectra when compared to the ATLAS but the profile or so as to say the distance between the lines will be conserved. This is very helpful in identifying lines. ECIDENTIFY is the task used to mark the lines. Once the lines are marked and the trend is identified, IRAF uses these calculations to convert the spectra in intensity v/s wavelength profile.

Continuum Fitting This task requires two procedures to be done before starting. Firstly it is required to the user to make several orders (around 127) of wavelength sections around 50 Å each with 5 such unit overlap between consecutive orders. The task SCOPY is applied where we specify the input spectra and get output cut section of wavelength region. It gives room to select start and end wavelength. Then we need to plot each order and manually remove spurious parts in the data that are not atomic lines but just noise peaks. Also stellar data is always absorption lines, we need to cut the noise peaks that appear like emission signatures. After this done for all orders we are ready to do continuum fitting. The aim of continuum fitting is to normalise the spectra, and set all the peaks to start from unity. Putting these atomic/molecular lines on the same normalised level is convenient to compare, locate wavelength and calculate equivalent width of each peak for further abundance analysis calculations. An example of FEROS spectrum of HD 179832 in Figure 3.3 illustrates this well.

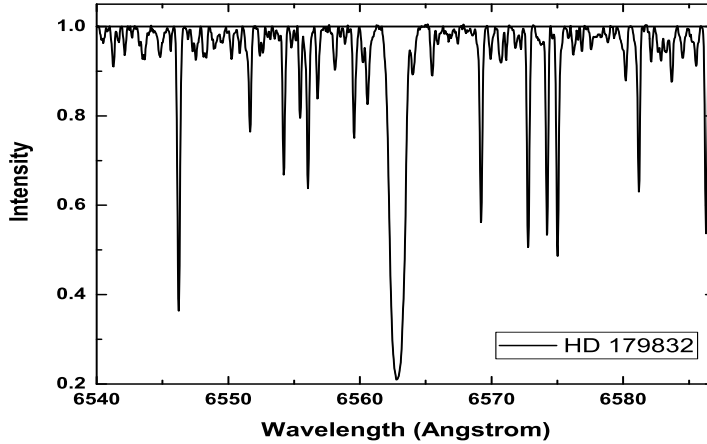


Figure 3.3: A sample of our continuum fitted spectra with continuum drawn.

3.3 Data Analysis

Once the spectra is reduced to its final form, the further measurements and the information to be extracted is explained in this section.

3.3.1 Radial Velocity Measurement

The object under study is part of our galactic system so it definitely has a radial velocity associated with it. Such a property is evidently entered into the spectra received during observation as each line is shifted by the some amount in a particular fixed direction.

To estimate the radial velocity we take fair number of clean Iron or Titanium lines in the spectra in every 1000 Å and find average shift in them with respect to the laboratory wavelength. For the rest frame wavelength we use Arcturus spectra as template. The object Arcturus is chosen so as to have a homogeneity in the analysis as it belongs giant class and has comparable temperature as the objects under study. The radial velocity formula is as follows:

$$V_r = \left(\frac{\lambda_{obs} - \lambda_{lab}}{\lambda_{lab}} \right) \times c \quad (3.1)$$

where c is the speed of light. In FEROS spectra of HD 179832, the pipeline already took care of the radial velocity corrections however it was still made accurate applying IRAF tasks like `rvcorrect` and `spectshift`. For programme stars HD 145777 and HE 2144-1832 we used the above discussed technique to calculate

the shifts and the calculated radial velocities are given in Table 4.3. We also use FXCOR package to cross check these calculations over the whole spectrum and found them to be consistent. Below is a figure showing programmed star spectra and Arcturus reference spectra in red.

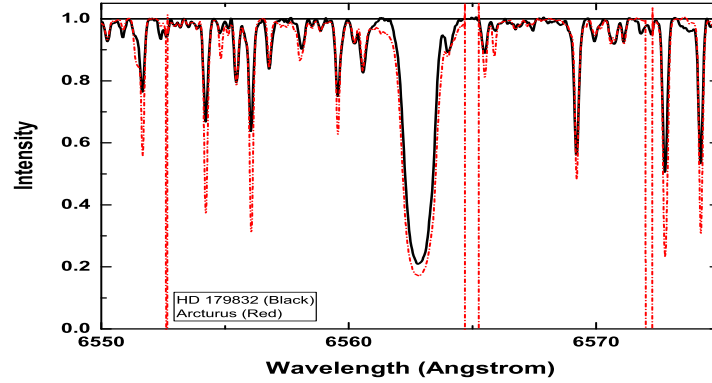


Figure 3.4: Our spectra(black) overplotted with reference Arcturus spectra(red)

3.3.2 Kurucz Model Atmosphere

Kurucz model atmosphere [51, 52, 53, 54] is a 1D model that mimics the properties of the photosphere to be able to infer the information from the spectral lines. Basically it's key role is to provide automated tables of quantities like electron number density ($N_e(\tau)$), opacity ($\kappa_\nu(\tau)$) density ($\rho(\tau)$), temperature ($T(\tau)$), pressure ($P(\tau)$), Note that these variables are calculated and listed as a function of optical depth(τ). This code generates model grid in ranges $3500 \text{ K} < T_{eff} < 7000 \text{ K}$; $0.0 < \log g < 5.0$; $-4.0 < [\text{Fe}/\text{H}] < 0.5$. It's key assumptions are:

- **Local Thermodynamic Equilibrium (LTE)** : This condition allows a gradient of temperature with space but the rate of change of temperature at a fixed point is zero.

$$\frac{\partial T(x)}{\partial t} = 0 \quad (3.2)$$

- **72 layers of plane-parallel atmosphere** : This means that the photosphere is modelled as a plane-parallel geometry meaning the thickness of the layer is very less compared to the radius of the star ($t \ll R$). Also this means that all the variables mentioned above are a function of only one space coordinate.

- **Radiative equilibrium** : This ensures that the net energy generation coming from below the layers of the atmosphere and none is transferred from outside. The equation of energy generation is:

$$\frac{dL}{dm} = \epsilon \quad (3.3)$$

and this is transferred as luminosity (L) which is constant.

- **Hydrostatic equilibrium** : This implies there is no net movement of the layers in the z (outward) direction i.e. no net acceleration.

$$\rho \frac{d^2r}{dt^2} = -\rho g + \frac{dP}{dr} = 0 \quad (3.4)$$

Equation of mass conservation:

$$\frac{dr}{dm} = \frac{1}{4\pi r^2 \rho} \quad (3.5)$$

3.3.3 MOOG

MOOG [77] is a Fortran based abundance analysis code (<http://www.as.utexas.edu/~chris/moog.html>) which works in LTE assumptions. It follows Edmonds (1969) formulation of stellar equations. We use this to compute light and heavy element abundances. This code takes as input the equivalent width of the neutral and ionized species from the light and heavy elements line-list and using the previously determined model atmosphere parameters and solving for the equations 3.6-3.8, applying curve of growth method to generate the output for corresponding abundances. In the fine line analysis mode we use an iterative method to remove lines with absurd/very off abundances to bring down standard deviation below 0.2 i.e. around the mean abundances for each element. In this procedure as well we use lines with equivalent width 20 - 180 mÅ as this range is not affected by micro-turbulence effects and damping constants.

Saha Equation:

$$\frac{n_1}{n_0} = \frac{1}{P_e} \left(\frac{(2\pi m_e)^{3/2} (kT)^{5/2}}{h^3} \right) \frac{2U_1(T)}{U_0(T)} e^{-\chi/kT} \quad (3.6)$$

Boltzmann Equation

$$\frac{N_b}{N_a} = \left(\frac{g_b}{g_a} \right) e^{-(E_b - E_a/kT)} \quad (3.7)$$

Abundance equation (Curve of growth analysis):

$$\log\left(\frac{W_\lambda}{\lambda}\right) = \log\left(\frac{\pi e^2 N_i N_H}{m_e c^2 U(T)}\right) + \log A + \log(gf \cdot \lambda) - \left(\frac{5040}{T}\right)\chi - \log(\kappa_\nu) \quad (3.8)$$

where

κ_ν is opacity; $\log(gf)$ is transition probability; A is the number abundance for element X relative to Hydrogen; $U(T)$ is Partition function used to calculate excitation and ionization.

3.3.4 Line analysis

There are four parts of doing the line analysis.

- **Line identification** : The very first task in hand after the IRAF reduced and radial velocity corrected spectra obtained is to identify clean, unblended and symmetric Iron absorption lines and prepare a master line list containing the wavelength corresponding to the line in the lab wavelength along with its $\log gf$ (Transition probability), excitation potential values, atomic number and equivalent width. We identify the lines using a reference lab wavelength shifted spectra of a well studied object (Arcturus) and over-plotting it against the our spectrum of the programme star. The laboratory wavelength used are those of the Kurucz database of atomic line lists. A master line-list of Fe I and Fe II elements is attached in the appendix.

- **Equivalent width measurement** :

The equivalent width is the measure of strength of the line defined as width of a rectangle (between 0 and 1) with the same area as of the continuum fitted line on a plot of intensity v/s wavelength scale. This illustrated in below. The equivalent width is of the order of mÅ.

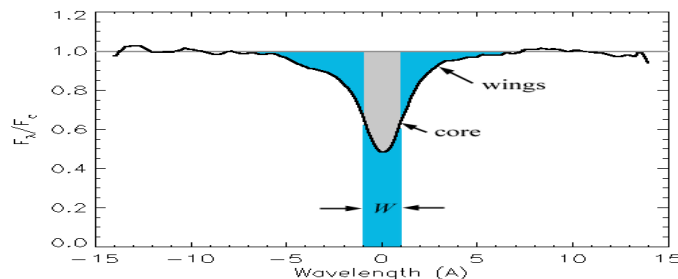


Figure 3.5: Absorption line showing equivalent width.
Image Source: <http://www.bdnyc.org/2012/03/02>

- **Deriving atmospheric parameters :** Using the line-list obtained as input in MOOG, we first derive abundances of Fe I and Fe II lines. Now to fix the spectroscopic temperature we iteratively solve for a value of it which gives the excitation potential balances amongst the used lines. For surface gravity under LTE conditions we use the fact that an element should give same abundance in different ionization states. So we solve for a model generated by Kurucz iteratively, which will give the ionisation balance represented by equation 3.8. To find the micro-turbulent velocity we repeat the same procedure find the balance between the equivalent width v/s Fe abundance. Figure 3.6-3.8 represents this very well where we solve for these atmospheric parameters to fix the surface temperature, surface gravity and micro-turbulent velocity for the program stars. Note that these iterative process has to be followed for each parameter simultaneously.

T_{eff} condition

$$\left. \frac{d(\log \epsilon)}{d\chi} \right|_{T_{\text{eff}}} = 0 \quad (3.9)$$

log g condition

$$\log \epsilon(\text{Fe I}) = \log \epsilon(\text{Fe II}) \quad (3.10)$$

Micro-turbulent velocity condition

$$\left. \frac{d(\log \epsilon)}{dw_{\lambda}} \right|_{v_t} = 0 \quad (3.11)$$

- **Estimation of elemental abundances :** This procedure has two parts. The first one is the Fine-line analysis method where we use equivalent width measurements of the elemental atomic lines to estimate the abundances. The idea is very similar to how we made the Fe line-list. This analysis gives the best estimate for lines with equivalent width in the range 20-180 mÅ.

A few lines because of the wavelength region they are found in or because of odd Z hyperfine splitting effects, are affected which may lead to either over or underestimation of their elemental abundances. In such cases we use spectrum synthesis method where we computationally generate the spectral line to match the observed one by iteratively solving for abundance. We show the spectral synthesis plots and abundance estimates for elements like Ba, Cu, Eu, La, Mn, O, Sc, V and few C₂, CN bands in the results section.

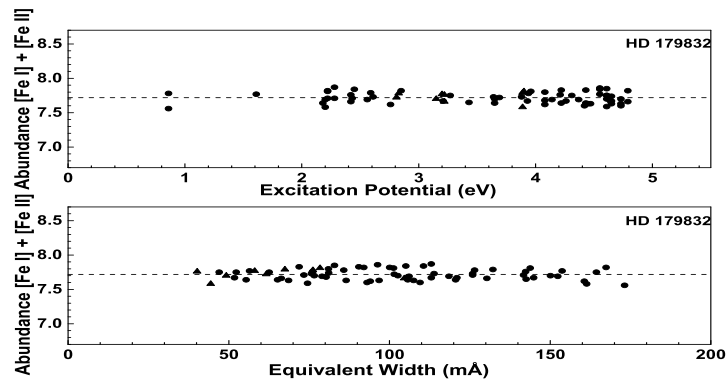


Figure 3.6: Excitation and Equivalent width balance in HD 179832

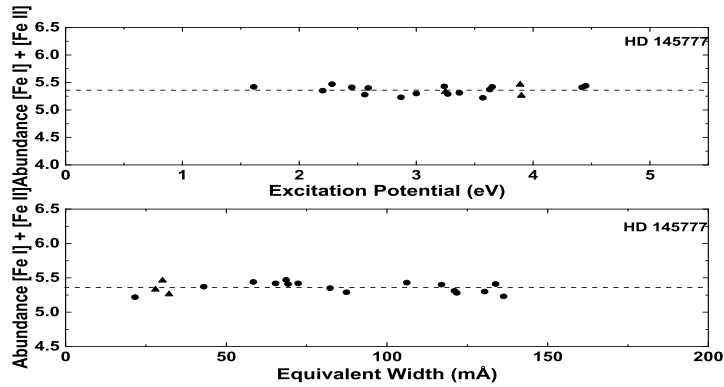


Figure 3.7: Excitation and Equivalent width balance in HD 145777

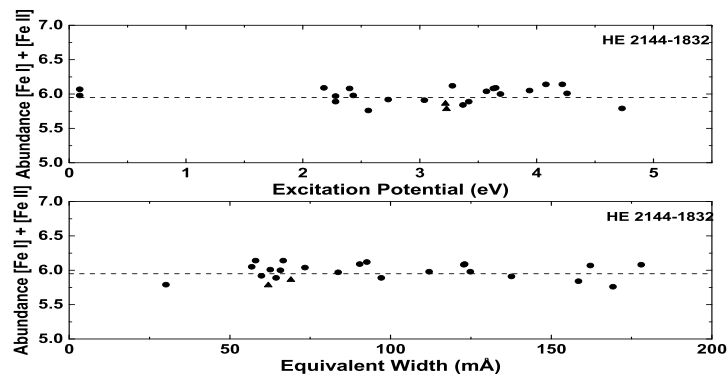


Figure 3.8: Excitation and Equivalent width balance in HE 2144-1832

Chapter 4

Results and Discussion

In this section we provide detailed results of the Photometric estimates, Atmospheric parameters, Chemical abundances, Mass, Age and Kinematic properties of the programme stars. Then further we do a comparative analysis of our final results with the respective existing literature to establish our findings.

4.1 Basic star data

Table 4.1 mentions some of the basic data of the programme stars which are used in the calculations. The data is taken from Simbad and the parallax data is taken from GAIA archive. The radial velocities and heliocentric correction are obtained from our analysis and compared to literature values.

Table 4.1: Basic data for the program stars. Source: Simbad Database

Star Name	HD 179832	HD 145777	HE 2144-1832
RA (2000)	19 16 30.00	16 13 13.87	21 46 54.67
DEC (2000)	-49 13 13.01	-15 12 01.245	-18 18 15.51
Proper Motion (μ_α) (mas/yr)	3.56 \pm 0.87	-12.952 \pm 0.21	-18.671 \pm 2.41
Proper Motion (μ_β) (mas/yr)	-12.52 \pm 0.64	-7.682 \pm 0.14	-12.189 \pm 2.55
Parallax (mas)	2.63 \pm 0.88	0.29 \pm 0.24	1.2 \pm 0.61
Radial velocity (km/s)	6.7 \pm 0.30	16.19 \pm 0.36	137.8 \pm 1.94
Heliocentric correction (km/s)	-3.89	-3.46	-29.76
Spectral Type	K0 III	C D	-

We provide different flux band values of the programme stars taken from Simbad database. These fluxes such as B,V,J,H,K are used in calculations of photometric temperature estimates and bolometric magnitude determination. The errors in the value are mentioned therein.

Table 4.2: Fluxes in different bands. Source: Simbad Database

Flux band	HD 179832	HD 145777	HE 2144-1832
B	9.46 ± 0.02	11.55 ± 0.12	12.651 ± 0.002
V	8.44 ± 0.01	10.31 ± 0.05	10.97 ± 0.1
R	-	-	10.471 ± 0.001
I	-	-	9.86 ± 0.001
G	-	9.748 ± 0.001	10.583 ± 0.001
J	6.66 ± 0.024	7.734 ± 0.027	8.768 ± 0.021
H	6.163 ± 0.027	7.067 ± 0.057	8.18 ± 0.026
K	6.031 ± 0.026	6.835 ± 0.02	7.958 ± 0.02

Table 4.3 produces radial velocity estimates this work produced compared to the literature values within the error. We used both manual line to line shift measurement and fxcor package to get our results. We do not have any literature estimate for HD 179832 but the other two objects have a good estimate of radial velocity with $|\Delta V_r|_{\text{observed-literature}}$ being <1 km/s for HD 145777 and <4 km/s for HE 2144-1832.

Table 4.3: Radial velocities V_r of the programme stars

Star Name	V_r (km/s) (This work)	S/N at 5500Å ^o	Date of Observation	V_r (km/s) (Literature)	References
HD 179832	6.7 ± 0.30	42.40	14/07/2000 (FEROS)	-	-
HD 145777	16.19 ± 0.36	19.88	01/06/2017 (HESP)	15 ± 4.7	Gontcharov 2006
HE 2144-1832	137.8 ± 1.94	21.62	08/11/2017 (HESP)	141.79 ± 1.0	Goswami 2005

4.2 Photometric Temperature Estimates

To determine spectroscopic temperature, we need a guess value to start with for the subsequent iterations. There is an Infra-red flux method [6] developed for calculating photometry temperatures using monochromatic fluxes from photometry observations and theoretical Kurucz model atmospheric flux distributions [51, 52]. These calculation provides a temperature estimate which is the guess around which spectroscopic temperatures are determined. The calculations for this photometric temperature estimates needs metallicity, so we divided temperature estimates into bins of 0.5 metallicity. For each programme star we calculate (J-H), (V-K) and (B-V) temperatures in range $-2.5 \leq [\text{Fe}/\text{H}] \leq 0$. (J-K) temperatures are independent of metallicity. The uncertainty in these temperatures is ~ 90 K.

Table 4.4: Photometric estimates of programme stars for $[\text{Fe}/\text{H}] \leq 0$

Star Name	Teff	Teff	Teff	Teff	Teff	Teff	Teff
Metallicity		0	0	0	-0.5	-0.5	-0.5
Flux band	(J-K)	(J-H)	(V-K)	(B-V)	(J-H)	(V-K)	(B-V)
HD 179832	4646	4651	4585	4615	4668	4565	4490
HD 145777	3839	3982	3638	4156	3998	3615	4047
HE 2144-1832	4076	4280	4008	3459	4297	3986	3374

Table 4.5: Photometric estimates of programme stars for $[\text{Fe}/\text{H}] \leq -1$

Star Name	Teff	Teff	Teff	Teff	Teff	Teff
Metallicity	-1	-1	-1	-1.5	-1.5	-1.5
Flux band	(J-H)	(V-K)	(B-V)	(J-H)	(V-K)	(B-V)
HD 179832	4684	4550	4392	4701	4540	4319
HD 145777	4015	3595	3961	4031	3577	3895
HE 2144-1832	4313	3967	3305	4330	3951	3250

Table 4.6: Photometric estimates of programme stars for $[\text{Fe}/\text{H}] \leq -2$

Star Name	Teff	Teff	Teff	Teff	Teff	Teff
Metallicity	-2	-2	-2	-2.5	-2.5	-2.5
Flux band	(J-H)	(V-K)	(B-V)	(J-H)	(V-K)	(B-V)
HD 179832	4718	4533	4268	4736	4531	4238
HD 145777	4048	3562	3847	4064	3550	3817
HE 2144-1832	4347	3939	3208	4364	3930	3179

All spectroscopic temperatures are quite near to the photometric estimates within their respective errors. $|\Delta T_{eff}|_{photometry-spectroscopy}$ for HD 179832 is < 130 K, for HE 2144-1832 being < 70 K. For HD 145777 this values is around 700K. We speculate the reason to be that the calculations which might not be that sensitive for cooler temperature and Very metal-poor (VMP) stars.

4.3 Atmospheric parameters

In this section we present the results of the derived model atmospheric parameters such as effective temperature T_{eff} , the surface gravity ($\log g$), micro- turbulent velocity (ζ), and metallicity [Fe/H] along with its errors.

For any chemical abundance analysis the effective temperature T_{eff} , the surface gravity ($\log g$), micro- turbulent velocity (ζ), and the metallicity [Fe/H] are the basic requirements. To determine this we need to computationally create the same model atmosphere which would produces lines with the observed properties given as input. For this we use Kurucz grid of model atmospheres (as discussed in subsection 3.3.2). We use this Fortran based code which solves for radiative transfer equations in Local Thermodynamic Equilibrium conditions to provide a suitable model with microscopic and macroscopic properties such as pressure, Rosseland mean opacity, electron density, micro-turbulent velocity and so on for the input effective temperature, surface gravity, micro-turbulent velocity, and the metallicity. Using this fixed model and again assuming LTE conditions we calculate for atmospheric parameters with input as Fe I and Fe II lines with excitation potential in the range 0-6 eV and equivalent width 20-180 mÅ. The underlying physics is that the strength of a spectral line depends on the number of atoms of that species undergoing transitions which provides the abundance output.

Table 4.7: Spectroscopic Atmospheric parameters results

Star Name	T_{eff} (K)	$\log g$ (g/cm^{-2})	ζ (Km/s)	[Fe I/H]	[Fe II/H]
HD 179832	4780 \pm 150	2.70 \pm 0.25	1.12 \pm 0.05	0.22 \pm 0.05	0.23 \pm 0.07
HD 145777	4750 \pm 150	0.40 \pm 0.25	2.67 \pm 0.05	-2.14 \pm 0.06	-2.15 \pm 0.10
HE 2144-1832	4260 \pm 150	0.70 \pm 0.25	2.06 \pm 0.05	-1.58 \pm 0.06	-1.61 \pm 0.09

4.4 Chemical abundances

In this section we present the abundances of elements such as C, N, O, Na, Mg, Ca, Sc, Ti, V, Cr, Mn, Ni, Cu, Zn, Sr, Y, Zr, Ba, La, Ce, Pr, Nd, Sm and Eu which are estimated and presented in Table 4.8-4.10 along with solar values by Asplund 2009 [9] and corresponding error ranges. The synthetic spectrum analysis plots and results are also presented below. The error for synthesis is taken to be ± 0.2 dex for each element. These results are also mentioned in Table 4.9 Table 4.9 and Table 4.11

Synthetic spectra plots: HD 179832

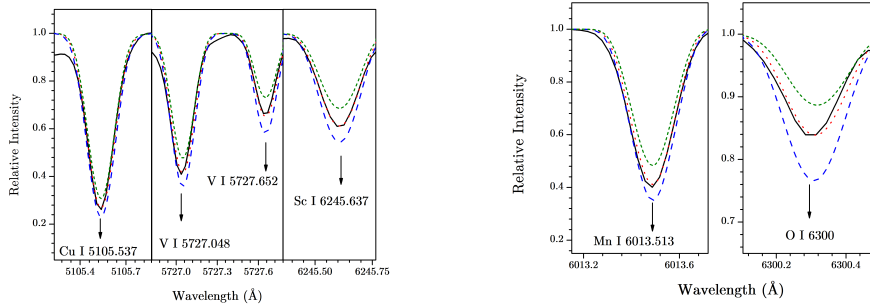


Figure 4.1: Left panel shows light elements(Cu, V and Sc) plots generated using spectral synthesis method and right panel shows the same for Mn and O. The green, red and blue lines represent the synthesized spectra. The top(green) and the bottom(blue) lines are enclosing the observed(black) spectra within $[X/Fe]=+0.3$. These are computed to show sensitive nature of atomic line with abundance.

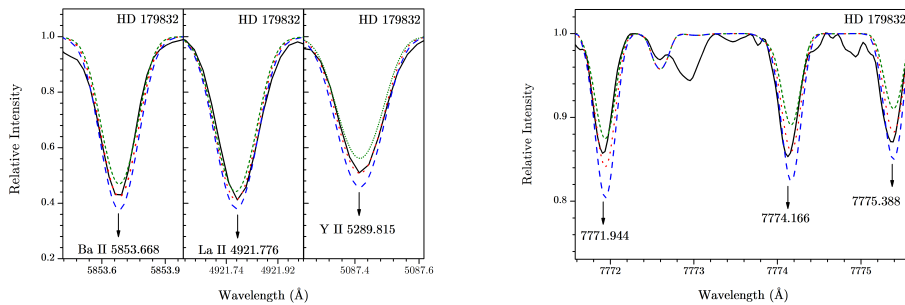


Figure 4.2: Left panel shows heavy elements(Ba, La and Y) plots generated using spectral synthesis method and right panel shows the same for Oxygen triplet. The green, red and blue lines represent the synthesized spectra. The top(green) and the bottom(blue) lines are enclosing the observed(black) spectra within $[X/Fe]=+0.3$. These are computed to show sensitive nature of atomic line with abundance.

Synthetic spectra plots: HD 145777

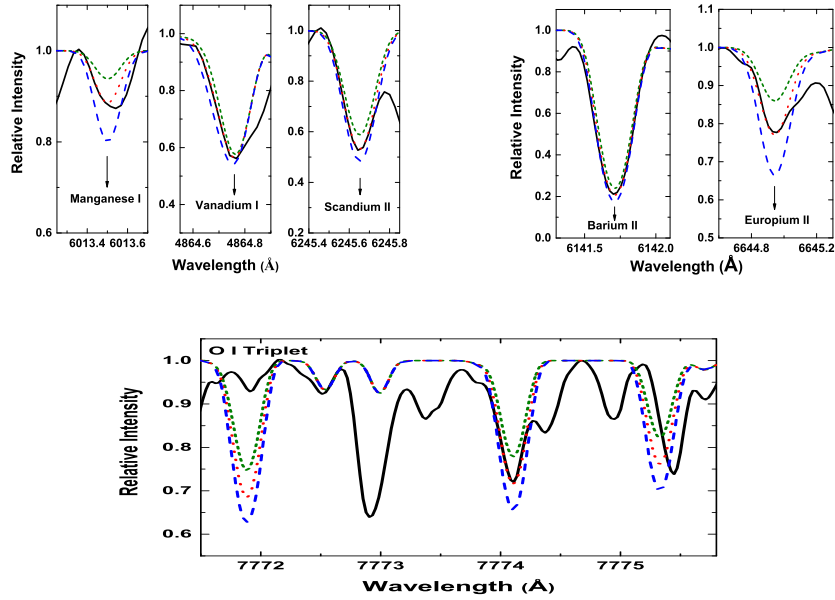


Figure 4.3: Left panel shows light elements(Mn, V and Sc) plots generated using spectral synthesis method and right panel shows the same for heavy elements (Ba and Eu); and Oxygen triplet (down). The green, red and blue lines represent the synthesized spectra. The top(green) and the bottom(blue) lines are enclosing the observed(black) spectra within $[X/Fe]=+0.3$. These are computed to show sensitive nature of atomic line with abundance.

Synthetic spectra plots: HE 2144-1832

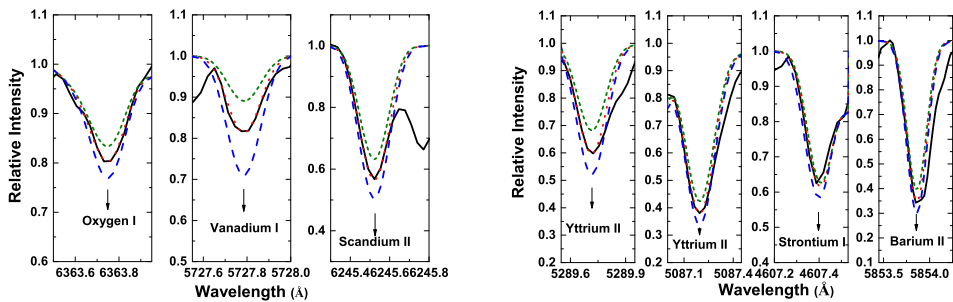


Figure 4.4: Left panel shows light elements(O, V and Sc) plots generated using spectral synthesis method and right panel shows the same for heavy elements (Y, Sr and Ba). The green, red and blue lines represent the synthesized spectra. The top(green) and the bottom(blue) lines are enclosing the observed(black) spectra within $[X/Fe]=+0.3$. These are computed to show sensitive nature of atomic line with abundance.

Table 4.8: Light elements abundances[X/Fe] and C/O ratio

Element	HD 179832	HD 145777	HE 2144-1832
C	-0.25 ±0.20	1.67 ±0.20	2.11 ±0.20
N	0.15 ±0.20	1.11 ±0.20	0.47 ±0.20
O	0.39 ±0.20	1.32 ±0.20	0.89 ±0.20
C/O	0.13	3.39	3.31

4.4.1 HD 179832

Table 4.9: Equivalent width and spectrum synthesis analysis results: HD 179832

Element	Z	$\log \epsilon_{\odot}^*$	$\log \epsilon$	Lines	σ	[X/H]	[X/Fe]
Light Elements							
O I	8	8.69 ± 0.05	9.31 ± 0.10	4	0.2	0.62 ± 0.11	0.40 ± 0.12
O I *	8	8.69 ± 0.05	9.3	syn		0.61	0.39 ± 0.20
Na I	11	6.24 ± 0.04	6.64 ± 0.13	2	0.18	0.4 ± 0.13	0.18 ± 0.14
Mg I	12	7.60 ± 0.04	7.41 ± 0	1	0	-0.19 ± 0.04	-0.41 ± 0.06
Si I	14	7.51 ± 0.03	7.7 ± 0.06	4	0.12	0.19 ± 0.07	-0.03 ± 0.08
Ca I	20	6.34 ± 0.04	6.4 ± 0.05	10	0.15	0.060 ± 0.06	-0.16 ± 0.07
Sc II	21	3.15 ± 0.04	3.48 ± 0	1	0	0.33 ± 0.04	0.11 ± 0.06
Sc II *	21	3.15 ± 0.04	3.35	syn		0.2	-0.02 ± 0.20
Ti I	22	4.95 ± 0.05	5.51 ± 0.07	7	0.18	0.56 ± 0.08	0.34 ± 0.09
Ti II	22	4.95 ± 0.05	5.51 ± 0.06	4	0.11	0.56 ± 0.07	0.34 ± 0.08
V I	23	3.93 ± 0.08	4.12 ± 0.20	3	0.35	0.19 ± 0.22	-0.03 ± 0.22
V I *	23	3.93 ± 0.08	4.1	syn		0.17	-0.05 ± 0.20
V II *	23	3.93 ± 0.08	4.1	syn		0.17	-0.05 ± 0.20
Cr I	24	5.64 ± 0.04	5.78 ± 0.02	3	0.03	0.140 ± 0.04	-0.08 ± 0.06
Cr II	24	5.64 ± 0.04	5.83 ± 0.02	2	0.03	0.19 ± 0.05	-0.03 ± 0.06
Mn I	25	5.43 ± 0.05	5.68 ± 0.05	3	0.08	0.25 ± 0.07	0.03 ± 0.08
Mn I *	25	5.43 ± 0.05	5.32	syn		-0.11	-0.33 ± 0.20
Co I	27	4.99 ± 0.07	5.31 ± 0.07	7	0.19	0.32 ± 0.10	0.10 ± 0.11
Ni I	28	6.22 ± 0.04	6.52 ± 0.06	13	0.2	0.3 ± 0.07	0.08 ± 0.08
Cu I *	29	4.19 ± 0.04	4.72	syn		0.53	0.31 ± 0.20
Zn I	30	4.56 ± 0.05	4.98 ± 0.11	2	0.15	0.42 ± 0.12	0.2 ± 0.12
Heavy Elements							
Sr I	38	2.87 ± 0.07	3.21 ± 0	1	0	0.34 ± 0.07	0.12 ± 0.08
Sr I *	38	2.87 ± 0.07	2.95	syn		0.08	-0.14 ± 0.20
Y II	39	2.21 ± 0.05	2.61 ± 0.06	5	0.13	0.4 ± 0.08	0.18 ± 0.09
Y II *	39	2.21 ± 0.05	2.45	syn		0.24	0.02 ± 0.20
Y II *	39	2.21 ± 0.05	2.52	syn		0.31	0.09 ± 0.20
Zr I	40	2.58 ± 0.04	2.5 ± 0.04	3	0.07	-0.08 ± 0.06	-0.3 ± 0.07
Zr II	40	2.58 ± 0.04	3.94 ± 0.04	3	0.07	1.36 ± 0.06	1.14 ± 0.07
Ba II	56	2.18 ± 0.09	2.87 ± 0.03	2	0.04	0.69 ± 0.09	0.47 ± 0.10
Ba II *	56	2.18 ± 0.09	2.82	syn		0.64	0.42 ± 0.20
La II	57	1.1 ± 0.04	1.71 ± 0.05	3	0.09	0.61 ± 0.07	0.39 ± 0.08
La II *	57	1.1 ± 0.04	1.85	syn		0.75	0.53 ± 0.20
Ce II	58	1.58 ± 0.04	2.52 ± 0	1	0	0.94 ± 0.04	0.72 ± 0.06
Pr II	59	0.72 ± 0.04	1.27 ± 0.21	2	0.29	0.55 ± 0.21	0.33 ± 0.21
Nd II	60	1.42 ± 0.04	1.72 ± 0.16	6	0.38	0.3 ± 0.16	0.08 ± 0.17
Sm II	62	0.96 ± 0.04	1.95 ± 0.04	5	0.1	0.99 ± 0.06	0.77 ± 0.07
Eu II	63	0.52 ± 0.04	1.28 ± 0.10	2	0.14	0.76 ± 0.11	0.54 ± 0.11
Eu II *	63	0.52 ± 0.04	0.75	syn		0.23	0.01 ± 0.20
Dy II	66	1.1 ± 0.04	2.99 0	1	0	1.89 ± 0.04	1.67 ± 0.06

⁰*Synthesized element; * Asplund 2009

4.4.2 HD 145777

Table 4.10: Equivalent width and spectrum synthesis analysis results: HD 145777

Element	Z	$\log \epsilon_{\odot}^*$	$\log \epsilon$	Lines	σ	[X/H]	[X/Fe]
Light Elements							
O I	8	8.69 ± 0.05	7.32 ± 0.07	2	0.10	-1.37 ± 0.09	0.77 ± 0.10
O I *	8	8.69 ± 0.05	7.87	syn		-0.82	1.32 ± 0.20
Na I	11	6.24 ± 0.04	4.85 ± 0.08	2	0.12	-1.39 ± 0.09	0.75 ± 0.10
Mg I	12	7.60 ± 0.04	6.40 ± 0	1	0	-1.20 ± 0.04	0.94 ± 0.06
Al I	13	6.45 ± 0.03	7.39 ± 0	1	0	0.94 ± 0.03	3.08 ± 0.05
Si I	14	7.51 ± 0.03	8.02 ± 0	1	0	0.51 ± 0.03	2.65 ± 0.05
Ca I	20	6.34 ± 0.04	5.30 ± 0.09	7	0.24	-1.04 ± 0.10	1.10 ± 0.11
Sc II	21	3.15 ± 0.04	1.94 ± 0	1	0	-1.21 ± 0.04	0.93 ± 0.06
Sc II *	21	3.15 ± 0.04	1.50 \pm	syn		-1.65	0.49 ± 0.20
Ti I	22	4.95 ± 0.05	4.00 ± 0.04	2	0.06	-0.95 ± 0.07	1.19 ± 0.08
Ti II	22	4.95 ± 0.05	3.07 ± 0	1	0	-1.88 ± 0.05	0.26 ± 0.06
V I *	23	3.93 ± 0.08	2.20	syn		-1.73	0.41 ± 0.20
Cr I	24	5.64 ± 0.04	4.04 ± 0.06	3	0.11	-1.60 ± 0.08	0.54 ± 0.09
Mn I	25	5.43 ± 0.05	3.46 ± 0	1	0	-1.97 ± 0.05	0.17 ± 0.06
Mn I *	25	5.43 ± 0.05	3.48	syn		-1.95	0.19 ± 0.20
Co I	27	4.99 ± 0.07	3.97 ± 0	1	0	-1.02 ± 0.07	1.12 ± 0.08
Ni I	28	6.22 ± 0.04	4.65 ± 0.07	2	0.10	-1.57 ± 0.08	0.57 ± 0.09
Zn I	30	4.56 ± 0.05	2.79 ± 0.07	2	0.10	-1.77 ± 0.09	0.37 ± 0.10
Heavy Elements							
Sr I	38	2.87 ± 0.07	2.52 ± 0	1	0	-0.35 ± 0.07	1.79 ± 0.08
Y II	39	2.21 ± 0.05	0.63 ± 0.09	3	0.15	-1.58 ± 0.10	0.56 ± 0.11
Zr I	40	2.58 ± 0.04	2.20 ± 0	1	0	-0.38 ± 0.04	1.76 ± 0.06
Ba II *	56	2.18 ± 0.09	1.60	syn		-0.58	1.56 ± 0.20
La II	57	1.10 ± 0.04	0.66 ± 0	1	0	-0.44 ± 0.04	1.70 ± 0.06
Ce II	58	1.58 ± 0.04	1.18 ± 0.03	3	0.06	-0.40 ± 0.05	1.74 ± 0.07
Pr II	59	0.72 ± 0.04	0.49 ± 0	1	0	-0.23 ± 0.04	1.91 ± 0.06
Nd II	60	1.42 ± 0.04	0.26 ± 0.13	4	0.25	-1.16 ± 0.13	0.98 ± 0.14
Sm II	62	0.96 ± 0.04	0.43 ± 0	1	0	-0.53 ± 0.04	1.61 ± 0.06
Eu II	63	0.52 ± 0.04	-0.12 ± 0.05	2	0.07	-0.64 ± 0.06	1.50 ± 0.08
Eu II *	63	0.52 ± 0.04	-0.40	syn		-0.92	1.22 ± 0.20

⁰*Synthesized element; *Asplund 2009

4.4.3 HE 2144-1832

Table 4.11: Equivalent width and spectrum synthesis analysis results: HE 2144-1832

Element	Z	$\log \epsilon_{\odot}^*$	$\log \epsilon$	Lines	σ	[X/H]	[X/Fe]
Light Elements							
O I *	8	8.69 ± 0.05	7.98	syn		-0.71	0.89 ± 0.20
Na I	11	6.24 ± 0.04	4.90 ± 0.13	2	0.19	-1.34 ± 0.14	0.26 ± 0.15
Mg I	12	7.60 ± 0.04	6.57 ± 0.01	2	0.02	-1.03 ± 0.04	0.57 ± 0.06
Al I	13	6.45 ± 0.03	6.38 ± 0	1	0	-0.07 ± 0.03	1.53 ± 0.05
Si I	14	7.51 ± 0.03	7.51 ± 0	1	0	0 ± 0.03	1.60 ± 0.05
Ca I	20	6.34 ± 0.04	5.46 ± 0.06	5	0.14	-0.88 ± 0.07	0.72 ± 0.08
Sc II	21	3.15 ± 0.04	1.95 ± 0	1	0	-1.20 ± 0.04	0.40 ± 0.06
Sc II *	21	3.15 ± 0.04	1.70	syn		-1.45	0.15 ± 0.20
Ti I	22	4.95 ± 0.05	3.25 ± 0.12	3	0.21	-1.70 ± 0.13	-0.10 ± 0.14
Ti II	22	4.95 ± 0.05	3.27 ± 0.21	2	0.30	-1.68 ± 0.22	-0.08 ± 0.22
V I	23	3.93 ± 0.08	2.55 ± 0.01	2	0.02	-1.38 ± 0.08	0.22 ± 0.09
V I	23	3.93 ± 0.08	2.65			-1.28 ± 0.08	0.32 ± 0.09
Cr I	24	5.64 ± 0.04	3.56 ± 0.09	3	0.15	-2.08 ± 0.10	-0.48 ± 0.10
Cr II	24	5.64 ± 0.04					
Mn I	25	5.43 ± 0.05	3.32 ± 0.03	3	0.05	-2.11 ± 0.06	-0.51 ± 0.07
Co I	27	4.99 ± 0.07	3.40 ± 0	1	0	-1.59 ± 0.07	0.01 ± 0.08
Ni I	28	6.22 ± 0.04	3.94 ± 0.08	4	0.15	-2.28 ± 0.09	-0.68 ± 0.09
Zn I	30	4.56 ± 0.05	2.79 ± 0	1	0	-1.77 ± 0.05	-0.17 ± 0.06
Heavy Elements							
Sr I	38	2.87 ± 0.07	1.61 ± 0	1	0	-1.26 ± 0.07	0.34 ± 0.08
Y II	39	2.21 ± 0.05	1.53 ± 0.09	3	0.16	-0.68 ± 0.11	0.92 ± 0.11
Y II *	39	2.21 ± 0.05	1.52	syn		-0.69	0.91 ± 0.20
Zr I	40	2.58 ± 0.04	2.08 ± 0.06	3	0.11	-0.50 ± 0.08	1.10 ± 0.09
Ba II	56	2.18 ± 0.09	1.29 ± 0	1	0	-0.89 ± 0.09	0.71 ± 0.10
Ba II *	56	2.18 ± 0.09	1.30	syn		-0.88	0.72 ± 0.20
La II	57	1.10 ± 0.04	0.91 ± 0.03	2	0.04	-0.19 ± 0.05	1.41 ± 0.06
Ce II	58	1.58 ± 0.04	0.73 ± 0.09	3	0.16	-0.85 ± 0.10	0.75 ± 0.11
Pr II	59	0.72 ± 0.04	0.55 ± 0	1	0	-0.17 ± 0.04	1.43 ± 0.06
Nd II	60	1.42 ± 0.04	0.68 ± 0.05	8	0.14	-0.74 ± 0.06	0.86 ± 0.08
Nd II *	60	1.42 ± 0.04	0.68	syn		-0.74	0.86 ± 0.20
Sm II	62	0.96 ± 0.04	0.50 ± 0.10	3	0.17	-0.46 ± 0.11	1.14 ± 0.11
Eu II	63	0.52 ± 0.04	-0.30 ± 0	1	0	-0.82 ± 0.04	0.78 ± 0.06

⁰*Synthesized element; *Asplund 2009

Carbon, Nitrogen and Oxygen: For Carbon abundance C_2 band in wavelength range 5162-5166 Å is synthesized in all the stars. The CN band at 4210-4216 Å is used for estimating Nitrogen abundance. Also, 8001-8006 Å, CN band region is used to determine Nitrogen abundance once Carbon is fixed. For Oxygen, atomic lines at 6300 Å, 6363 Å as well as oxygen triplet is in 7770-7775 Å region are used. All these are estimated by spectral synthesis methods and the results are given in Table 4.9 and Table 4.11. Carbon is over-abundant ($[C/Fe]>1$) in CEMP stars HD 145777 and HE 2144-1832. Oxygen is over-abundant in HD 145777 and HE 2144-1832 whereas mild over abundant in HD 179832. This is the reason behind for the C/O ratio below unity for the HD 179832.

Odd Z elements Na and Al: Abundance of both Sodium and Aluminium both elements have been determined by Line analysis method. Sodium is estimated by two clean lines in each case. While $[Na/Fe] \geq 0.57$ in the CEMP objects, it is marginally over abundant in HD 179832 with $[Na/Fe]<0.20$. No Aluminium lines are found this object whereas $[Al/Fe]$ is absurdly high for HD 145777 and more than unity for HE 2144-1832.

α -elements Mg, Si, Ca and Ti: The α -elements are determined using only line analysis method. Magnesium is under-abundant in HD 179832 and over-abundant for the other two star with HD 145777 value almost nearing unity. Similar trend is observed in Silicon as well with HD 179832 showing near solar value and the other having $[Si/Fe] \geq 1.60$. HD 179832 is under-abundant in calcium while the other two are over-abundant with HD 145777 giving above unity value. Titanium is estimated using lines from both neutral and ionic species. It is over-abundant for HD 179832 and HD 145777, whereas HE 2144-1832 showing negative values indicating under-abundance.

Iron-peak elements Mn and Ni: Manganese abundance is determined with both line analysis and spectral synthesis method. The 6013 Å line is used to synthesize the spectral feature. For HE 2144-1832 the spectral synthesis analysis could not be done because of heavy blending by other lines. However line analysis gives an overestimated value to put an upper bound. Nickel is estimated with lines as many in the range from 2-13 in number varying across the programme star spectra. HE 2144-1832 shows under-abundance of both Manganese and Nickel. HD 179832 shows both under-abundance and over-abundance in Manganese and Nickel respectively with Nickel value being near solar. HD 145777 shows over-abundance in both the elements with $[X/Fe] \geq 0.17$ where $X=Mn, Ni$.

Light s-process elements Sr, Y and Zr: The light s-process neutron capture elemental abundances have been estimated using line analysis of respective atomic lines. For spectral synthesis method we use Sr I 4607 Å line and Y II 5087 Å, 5289 Å line. No Zirconium estimate could be made by line synthesis due to severe blending of 4205 Å and 4208 Å line by other transitions. Strontium shows near solar, high over-abundance and mild over-abundance for HD 179832, HD 145777 and HE 2144-1832 respectively. This shows an anti-correlation with observed metallicity which we will discuss later. Yttrium is again near solar for HD 179832 and over-abundant for the other two stars with value $[Y/Fe] \geq 0.56$ hence another element showed anti-correlation with observed metallicity. The exact same trend is followed in Zirconium too. The meta-rich HD 179832 has negative abundance and the other two have value $[Zr/Fe] \geq 1.10$. The abundance shown by HD 145777 is estimated with one line so the value is could have an offset but will definitely follow the anti-correlation trend.

Heavy s-process elements Ba, La, Ce, Nd and Eu: Barium being the key element, is enhanced in all three stars with $[Ba/Fe] \geq 0.42$. The synthesis method has been applied to all three objects using 5853 Å and 6141 Å line but no line was obtained for equivalent width line analysis in the most metal-poor star HD 145777. Rest have been analysed with 2 lines each. Lanthanum is estimated with 4921 Å line in the stars but this is heavily blended in HD 145777. This element is enhanced in all three objects but only HD 145777 passes unity. No synthesis of line is done for Cerium but use of at least 3 lines in line analysis gives statistically significant results. Cerium is almost similar for HD 179832 and HE 2144-1832 with $[Ce/Fe] \approx 0.73$. The remaining one yet again is enhanced above unity. There are enough lines measured for Neodymium which ranges from 4-8. Synthesis is only done for 5212 Å line in HE 2144-1832 which exactly matches with the line analysis results. HD 179832 and HD 145777 have abundances near solar and near unity respectively whereas HE 2144-1832 has value $[Nd/Fe] = 0.86$. The heavy s-process key element is Europium is enhanced in all three stars with line analysis method with lower limit of abundance being $[Eu/Fe] \geq 0.54$. Eu II lines such as 6437 Å and 6645 Å have been used to supplement the line analysis results. However HD 179832 produce near solar abundance with spectrum synthesis estimate whereas no proper estimate could be done in case of HE 2144-1832 due to severe blending.

4.5 Mass and age determination

To determine Mass and age of the programme stars we need to first calculate luminosity. For this we need to deduce Bolometric magnitude M_{bol} of the star which is given by the equation as follows:

$$M_{bol} = V - 5\log(d) + 5 - A_v + BC \quad (4.1)$$

where V is visual band flux adopted from Simbad database, d is the distance in parsec converted from the parallax value given by GAIA database, A_v is the extinction coefficient calculated using methods in Chen et al. [23] and BC is Bolometric correction is calculated using empirical calibrations in paper by Alonso et al. [6]. We present the tabulated results below.

Table 4.12: Distance, Bolometric correction, Extinction coefficient and Bolometric magnitude of the programme stars

Star Name	Distance (pc)	M_v	BC	A_v	M_{bol}
HD 179832	380.23 ± 127.23	0.54	-0.344 ± 0.001	0.039	0.16 ± 0.06
HD 145777	3448.28 ± 2853.75	-2.64	-0.380 ± 0.001	0.278	-3.02 ± 0.62
HE 2144-1832	833.33 ± 423.61	1.37	-0.644 ± 0.001	0.029	0.69 ± 0.22

Now that we have Bolometric magnitude, we can calculate luminosity ratio with respect to solar using the following relation:

$$\log\left(\frac{L}{L_{\odot}}\right) = \frac{M_{bol\odot} - M_{bol}}{2.5} \quad (4.2)$$

where $M_{bol\odot}$ is the solar bolometric magnitude is adopted to be 4.75 [26].

Using the calculated luminosities and the spectroscopic calculated effective temperatures we can locate the point on the evolutionary tracks and isochrones of stellar evolution models [31]. This data base of evolutionary tracks spans the range from $0.6M_{\odot} - 12.0M_{\odot}$ and Metallicity (Z) from 0.0004 – 0.03. These tracks and isochrones are generated for metallicity (Z) of the star which is given by the relation:

$$Z = \left(\frac{N_{Fe}}{N_H}\right)_* = \left(\frac{N_{Fe}}{N_H}\right)_{\odot} \times \text{antilog} [\text{Fe}/\text{H}]_* \quad (4.3)$$

where $\left(\frac{N_{Fe}}{N_H}\right)_{\odot} = 0.019$. The best suited models for HD 179832, HD 145777 and HE 2144-1832 were calculated to be 0.03, 0.0004 and 0.0004 respectively. The plots of the HR diagram tracks are shown in Figure 4.5 and Figure 4.6.

Calculations from Parallax Using inputs like Mass, Bolometric luminosity, T_{eff} from the above tables we can now determine the surface gravity of the star by the following relation:

$$\log\left(\frac{g}{g_{\odot}}\right) = \log\left(\frac{M}{M_{\odot}}\right) + 4\log\left(\frac{T_{eff}}{T_{eff_{\odot}}}\right) + 0.4(M_{bol} - M_{bol_{\odot}}) \quad (4.4)$$

where the solar values are adopted to be $M_{bol_{\odot}} = 4.75$; $T_{eff_{\odot}} = 5770$ K; $\log g_{\odot} = 4.44$ [26].

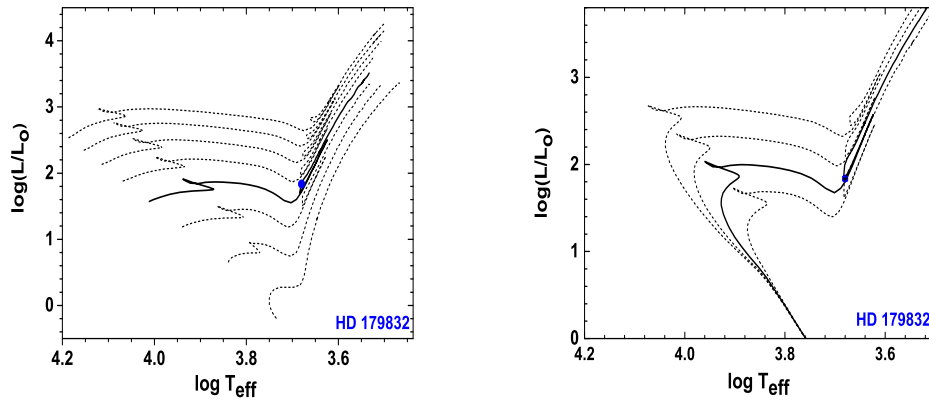


Figure 4.5: Location of HD 179832 in the H-R diagram. For mass estimate the evolutionary tracks are shown for 1, 1.5, 2, 2.5, 3, 3.5, 4 and 4.5 solar mass, from bottom to top (left). For age estimate the Isochrones are shown for log t 8.4, 8.6, 8.8,9.0 from top to bottom (right) The errors are small compared to the data point

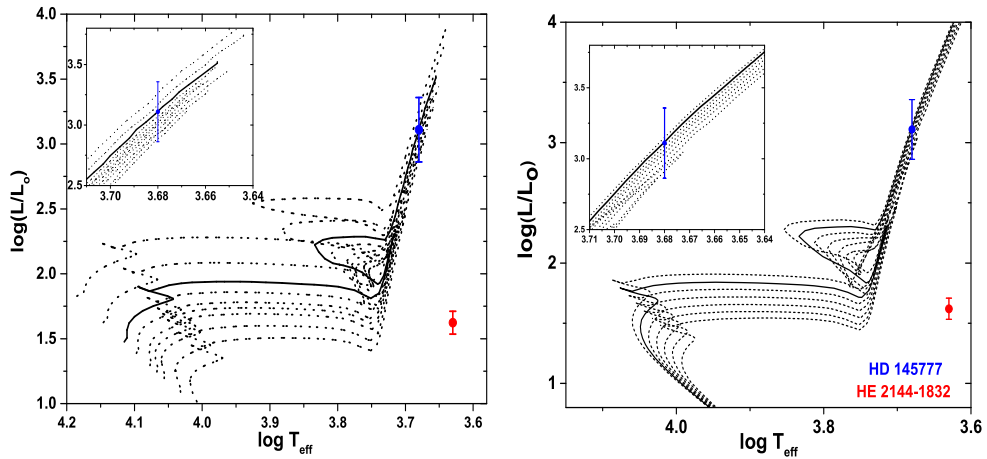


Figure 4.6: Location of HD 145777(red) and HE 2144-1832(blue) in the H-R diagram. For mass estimate the evolutionary tracks are shown for 1, 1.6, 1.7, 1.8, 1.9, 2.0, 2.2 and 2.5 solar mass, from bottom to top (left). For age estimate the Isochrones are shown for log t 8.4, 8.6, 8.8,9.0 from top to bottom (right).

Table 4.13: Calculations from Parallax

Star Name	$\log(L/L_{\odot})$	$\log(\text{Teff})$	Mass M_{\odot}	Age (Myr)	$\log g$
HD 179832	1.84 ± 0.04	3.68	2.50 ± 0.50	5.012×10^2	2.68 ± 0.20
HD 145777	3.11 ± 0.50	3.68	1.70 ± 1.50	7.943×10^2	0.88 ± 0.76
HE 2144-1832	1.62 ± 0.18	3.63	<2.60	-	-

We find the mass of the HD 179832 and HD 145777 to be $2.50 M_{\odot}$ and $1.70 M_{\odot}$ and ages 5.012×10^2 Myr and 7.943×10^2 Myr respectively. We could not locate the the mass and age of the object HE 2144-1832 because it does not intersect the theoretical evolutionary tracks and isochrones. Probably as it is clear from Figure 4.6 that it has cooler temperature and the theoretical models are not interpolated for the given metallicity. However we could derive from the y axis value of the point that the star has completed the Hydrogen burning in its main sequences and sub-giant phase almost ascending to the first giant branch phase. There are no direct theoretical approach to have a mass-luminosity or mass-radius relation as it exist for main sequence. Simply because of the sub-structure of the star is very complicated to model because of the expansion of the outer envelop and the discontinuous density gradients. We can broadly put an upper bound on the mass using the main sequence mass-luminosity relation. However within certain approximations and observational constraints there are methods [73] to model the core mass M_c in RGB phase from the luminosity of the star. We attempt to find that using the relation:

$$\frac{L}{L_{\odot}} = 200 \left(\frac{M_c}{0.3M_{\odot}} \right)^{7.6} ; 0.15 < M_c < 0.45 \quad (4.5)$$

We calculate the core mass to be $0.244 M_{\odot}$. We propose a core-envelop mass could provide a better upper bound on the total mass of the star. HD 179832 is also in the first giant branch whereas HD 145777 is well within the giant branch.

4.6 Kinematic analysis

The components of spatial velocity, total spatial velocity and probability for the star being member of a particular population are estimated and is given in Table 4.14 Table 4.15 and Table 4.16. Firstly we have to define the spatial components. The U_{LSR} , V_{LSR} and W_{LSR} correspond to component vectors in direction along axes pointing towards the Galactic center, the direction of Galactic rotation and the North Galactic Pole respectively. This is very much depiction in the Figure 4.7.

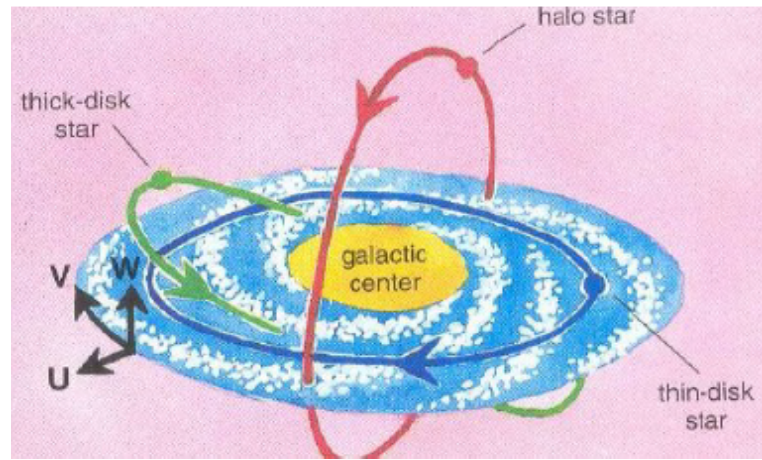


Figure 4.7: Image Reference: https://www3.nd.edu/~vplacco/talks/jina_vmp.pdf

The LSR stands for Local Standard of Rest. We use data for proper motions and distance from Simbad along with calculated radial velocity (V_r) to calculate these vectors using the method presented by Johnson & Soderblom [43]. The equation is given by this simple matrix:

$$\begin{bmatrix} U \\ V \\ W \end{bmatrix} = B \begin{bmatrix} V_r \\ k \cdot \mu_\alpha / \pi \\ k \cdot \mu_\delta / \pi \end{bmatrix}; k = 4.74057 \text{ km/s} \quad (4.6)$$

To calculate this we need to use matrix $B=T.A$, which is a transformation matrix. This transformation matrix connects the Galactic coordinate system and equatorial coordinate system. A is a coordinate matrix defined below

$$T = \begin{bmatrix} 0.06699 & 0.87276 & 0.48354 \\ 0.49273 & 0.45035 & 0.74458 \\ 0.86760 & 0.18837 & 0.46020 \end{bmatrix}; A = \begin{bmatrix} \text{Cos}\alpha \cdot \text{Cos}\delta & \text{Sin}\alpha & \text{Cos}\alpha \cdot \text{Sin}\delta \\ \text{Sin}\alpha \cdot \text{Cos}\delta & \text{Cos}\alpha & \text{Sin}\alpha \cdot \text{Sin}\delta \\ \text{Sin}\delta & 0 & \text{Cos}\delta \end{bmatrix}$$

Now we use another transformation where we use solar motion with respect to Local Standard of Rest as follows:

$$(U, V, W)_{LSR} = (U, V, W) + (U, V, W)_{\odot} \text{ km/s} \quad (4.7)$$

where $(U, V, W)_{\odot} = (11.1, 12.2, 7.3) \text{ km/s}$ [79].

Finally we calculate the spatial velocity using the relation:

$$V_{spa}^2 = U_{LSR}^2 + V_{LSR}^2 + W_{LSR}^2 \quad (4.8)$$

Table 4.14: Kinematic analysis results

Star Name	U_{LSR} (km/s)	V_{LSR} (km/s)	W_{LSR} (km/s)	V_{spa} (km/s)
HD 179832	8.26 ± 1.06	-7.98 ± 2.17	-6.14 ± 1.75	13.02 ± 2.98
HD 145777	-12.61 ± 33.86	-220.36 ± 191.88	86.12 ± 58.88	236.93 ± 203.550
HE 2144-1832	159.59 ± 37.21	30.02 ± 20.81	-58.9 ± 19.40	172.74 ± 46.84

Since we now have components of spatial velocity and total spatial velocity, we can also calculate the probability for the star to be a member of 3 defined populations. These are thin disk, thick disk and halo populations. We employ the well established method [72, 14, 15, 67] to calculate these probabilities. The pre-requisite is the Table 4.15 taken from Reddy et al. [72].

Table 4.15: Velocity dispersions, asymmetric drift velocities, and the fractional population of three stellar components.

Component	σ_U	σ_V	σ_W	V_{ad}	f
Thin	43	28	17	-9	0.93
Thick	67	51	42	-48	0.07
Halo	131	106	85	-220	0.006

Now we use the following equations and calculate the probabilistic distribution of the programme stars HD 179832, HD 145777 and HE 2144-1832.

$$P_{thin} = \frac{f_1 p_1}{P}; P_{thick} = \frac{f_2 p_2}{P}; P_{halo} = \frac{f_3 p_3}{P} \quad (4.9)$$

where

$$P = \sum f_i p_i$$

$$p_i = K_i \exp \left[-\frac{U_{LSR}^2}{2\sigma_{U_i}^2} - \frac{(V_{LSR} - V_{ad})^2}{2\sigma_{V_i}^2} - \frac{W_{LSR}^2}{2\sigma_{W_i}^2} \right] \quad (4.10)$$

$$K_i = \frac{1}{(2\pi)^{3/2} \cdot \sigma_{U_i} \cdot \sigma_{V_i} \cdot \sigma_{W_i}}; i = 1, 2, 3 \quad (4.11)$$

Table 4.16: Galactic Distribution Probability results

Star Name	P thin	P thick	P halo
HD 179832	0.992	0.008	≈ 0
HD 145777	≈ 0	0.060	0.940
HE 2144-1832	0.012	0.954	0.034

The results show that the objects HD 179832, HD 145777 and HE 2144-1832 and maximum probability of being a member of thin, halo and thick disk population respectively. The spatial velocities of these stars also validate these calculations.

4.7 Error Analysis

Equivalent width error in abundance.

$\sigma_{EW}=0.02$ dex (Cayrel 1988)

Atmospheric Parameters: The uncertainties are the minimum limit of interpolation of the parameters.

$\sigma_{T_{eff}}=150$ K; Abundance error=0.10 dex

$\sigma_{logg}=0.25$; Abundance error=0.02 dex

$\sigma_{\zeta}=0.05$; Abundance error=0.06 dex

All the error formulation below has been adopted from Allen et al. [4].

Parallax derived surface gravity:

$$\sigma_{logg} = \left[\sqrt{\left(\frac{\sigma_M}{M \ln(10)}\right)^2 + \left(\frac{4\sigma_{T_{eff}^*}}{T_{eff}^* \ln(10)}\right)^2 + \left(\frac{4\sigma_{T_{eff}^\odot}}{T_{eff}^\odot \ln(10)}\right)^2 + \sigma_{logg^\odot}^2 + (0.4\sigma_V)^2 + (0.4\sigma_{BC})^2 + \left(\frac{2\sigma_\pi}{\pi \ln(10)}\right)^2} \right]$$

Abundance:

$$\sigma_{\mathcal{E}(Fe)} = \sqrt{(\Delta\mathcal{E}(Fe)_{EW})^2 (\Delta\mathcal{E}(Fe)_{T_{eff}})^2 + (\Delta\mathcal{E}(Fe)_{logg})^2 + (\Delta\mathcal{E}(Fe)_\xi)^2}$$

$$\sigma_{[Fe/H]} = \sqrt{\sigma_{\log\mathcal{E}(Fe)}^2 + \sigma_{\log\mathcal{E}(Fe)^\odot}^2}$$

Absolute magnitude:

$$\sigma_{M_v} = \sqrt{(\sigma_V)^2 + \left(\frac{5\sigma_D}{D \ln(10)}\right)^2 + (\sigma_{A_v})^2}$$

Bolometric magnitude:

$$\sigma_{M_{bol}} = \sqrt{(\sigma_{M_v})^2 + (\sigma_{BC})^2}$$

Luminosity:

$$\sigma_L = (0.4L) \ln(10) \sqrt{(\sigma_{M_{bol*}})^2 + (\sigma_{M_{bol\odot}})^2}$$

4.8 Comparative studies

We have carried out an extensive survey of literature data for comparative analysis of properties such as metallicity, atmospheric parameters, mass and luminosity. Also comparative study has been extended to individual elemental species including Carbon, Nitrogen and Oxygen; Odd Z elements such as Sodium; α -elements such as Magnesium, Calcium and Titanium; Iron-peak elements such as Manganese and Nickel; Light s-process elements such as Strontium, and Yttrium; Heavy s-process elements such as Barium, Lanthanum, Cerium, Neodymium and Europium.

4.8.1 Atmospheric Parameters

We compare our atmospheric parameters and few other results with the literature survey of a large sample of Barium stars and CEMP stars. The preliminary test of the HD 179832 including the strength of 4554 Å Ba II line and C/O ratio puts it in the category of potential Barium stars. We use Barium star database of de Castro (2016) and literature therein. Similarly, C/O being more than unity for HD 145777 and HE 2144-1832 makes them potential CH star candidate and even lower metallicity $[\text{Fe}/\text{H}] < -1$ and Carbon enhancement $[\text{C}/\text{Fe}] > 1$ further classifies them in the category of Carbon Enhanced Metal-poor (CEMP) stars. Hence we use a large sample of CEMP stars [1, 2, 3, 5, 11, 25, 35, 37, 40, 62, 84]. We plot histogram of these parameters and obtain a Gaussian fit to estimate the peak value of the parameter and then compare it with our results. We notice that our values lie within the maximum to minimum frequency range of the corresponding parameters in both Barium star data as well as CEMP data in Figure 4.8 and Figure 4.9. HD 179832 is an exception in metallicity since the sample taken is mildly metal-poor.

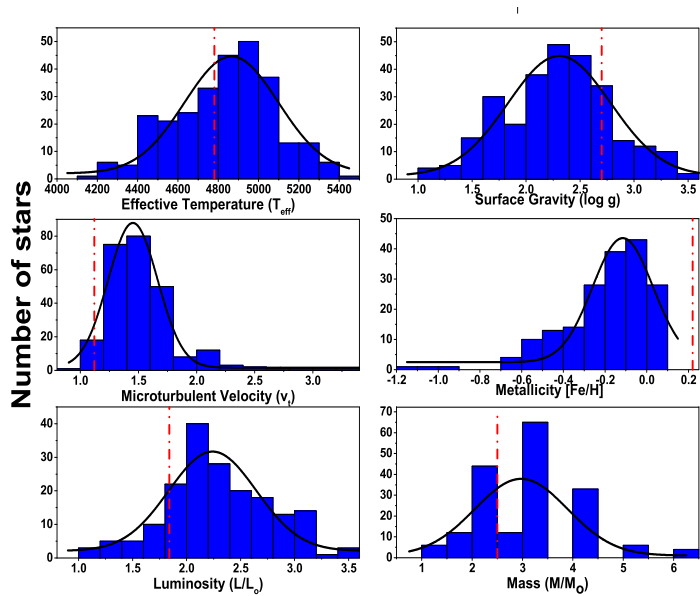


Figure 4.8: Comparison of HD 179832 with Barium star Literature (left). Data Source: de Castro 2016 and literature therein. Data Source: Masseron et al. (2010); Hansen et al. (2016); Goswami et al. (2016); Aoki et al. (2007); Abate et al. (2015); Allen et al. (2012); Goswami et al. (2006); Tsangarides et al. (2005); Barklem et al. (2005); Cohen et al. (2006)

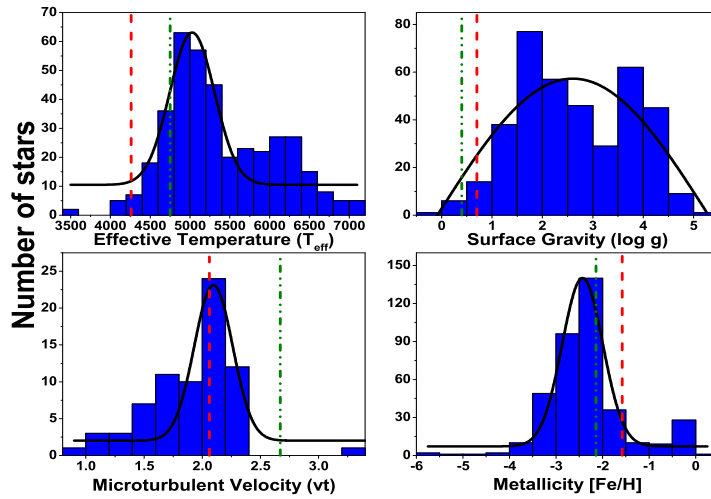


Figure 4.9: Comparison of HD 145777 and HE 2144-1832 with CEMP star Literature (right) Data Source: Masseron et al. (2010); Hansen et al. (2016); Goswami et al. (2016); Aoki et al. (2007); Abate et al. (2015); Allen et al. (2012); Goswami et al. (2006); Tsangarides et al. (2005); Barklem et al. (2005); Cohen et al. (2006)

4.8.2 Kinematics

Using the results obtained in section 4.6, we perform comparative analysis study for HD 179832, HD 145777 and HE 2144-1832. For the Barium star we use the homogeneous large sample of sample [27] and for the other two objects we use the metal-poor stars sample [13]. Figure 4.10, Figure 4.11 and Figure 4.12 has shows U_{LSR} , V_{LSR} and W_{LSR} plotted against metallicity for HD 145777 and HE 2144-1832. As mentioned previously these are component vectors in direction along anti-galactic centre, galactic rotation and galactic north pole respectively. In all three figures we see that the scatter in the values keeps increasing as we go along decreasing metallicity. Our objects lie well within the scatter at corresponding metallicity. The plots clearly show high value of galactic rotation vector in HD 145777 and anti-galactic centre component in HE 2144-1832.

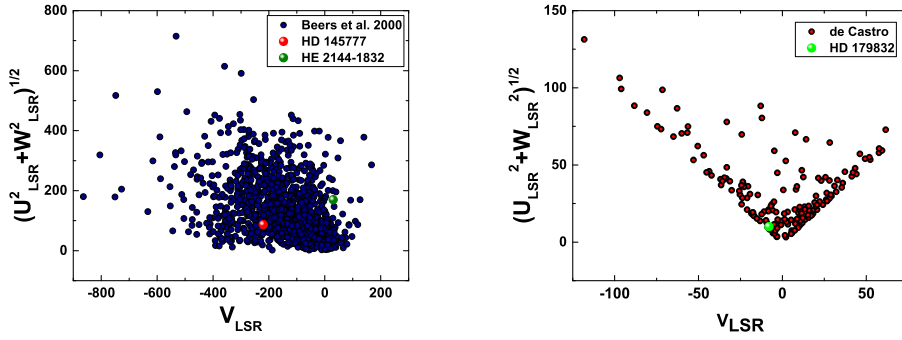


Figure 4.10: Toomre diagram for HD 145777, HE 2144-1832 (left) and HD 179832 (right) plotted with corresponding literature.

Figure 4.10 gives the Toomre diagram for HD 14577, HE 2144-1832 (left) and HD 179832 (right). It is the square root of the sum of the squares of both U_{LSR} and W_{LSR} against V_{LSR} . One can notice that the right panel clearly shows HD 179832 being close to the diverging point near zero which is the region for thin disk stars whereas the other two objects (left) lie farther away from disk region.

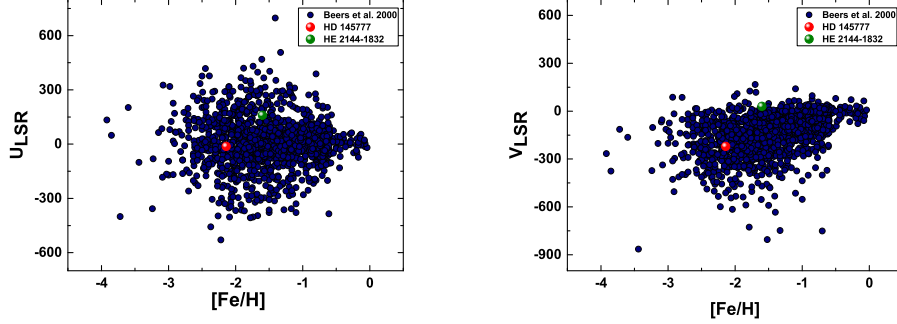


Figure 4.11: Metallicity of HD 145777 and HE 2144-1832 plotted against U_{LSR} (left) and V_{LSR} (right) along with literature data.

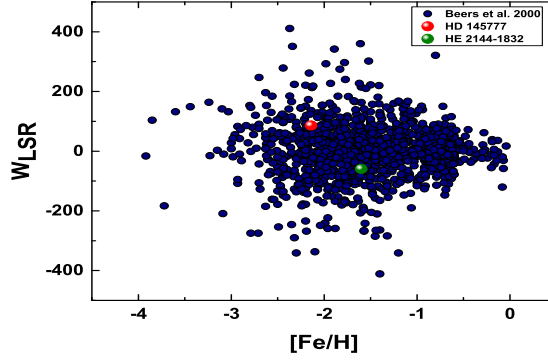


Figure 4.12: Metallicity of HD 145777 and HE 2144-1832 plotted against W_{LSR} along with literature data.

4.8.3 Chemical Abundances

Now we come to the individual element-wise analysis of the results presented in [section 4.4](#). For Barium stars we have divided the analysis into two parts. Firstly, we compare our results of light elements such as Na, Mg, Ca, Sc, Ti, V, Cr, Mn, Co, Ni and heavy elements such as Y, Ba, La, Ce, Nd, Eu with literature data of Barium giants (weak and strong); Barium dwarfs (weak and strong) and Barium subgiants. For this we refer to literature database [\[57, 85, 68\]](#). Then in the second part, we compare these elements with literature Barium stars [\[4, 27, 55, 50, 60, 87\]](#). We also compare metallicity trends of C, N, O abundances with existing literature. We do the same with CEMP stars and use a database containing both CEMP-s and CEMP-r/s stars in a large metallicity range. The literature referred is in the caption of [Figure 4.13- Figure 4.19](#).

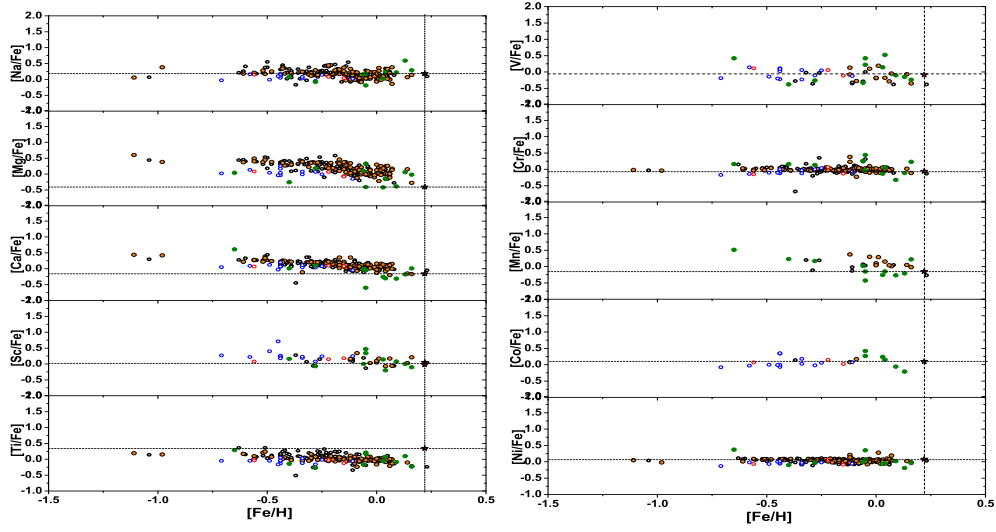


Figure 4.13: Comparison of light elements in HD 179832 with Barium stars in literature Data source: Yang et al 2016; de Castro et al. 2016; Allen & Barbuy 2006; Liang 2003; Mahanta U. et al. 2016; Karinkuzhi et al. 2018. Strong Ba giants (black); weak Ba giants(orange); Ba dwarf(blue); Ba subgiants(red); Normal Ba stars(green); HD 179832(pink).

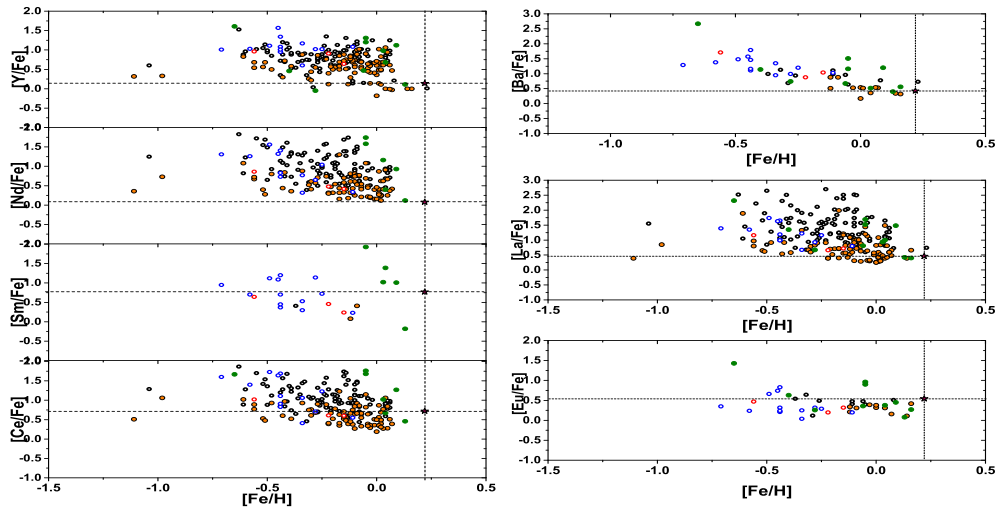


Figure 4.14: Comparison of heavy elements in HD 179832 with Barium stars in literature Data source: Yang et al 2016; de Castro et al. 2016; Allen & Barbuy 2006; Liang 2003; Mahanta U. et al. 2016; Karinkuzhi et al. 2018. Strong Ba giants (black); weak Ba giants(orange); Ba dwarf(blue); Ba subgiants(red); Normal Ba stars(green); HD 179832(pink).

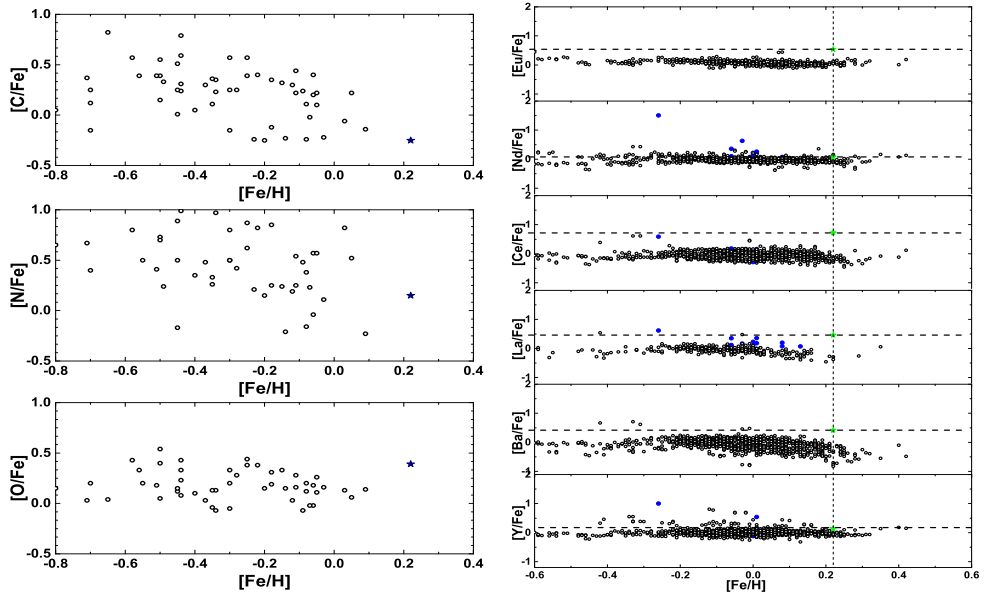


Figure 4.15: Comparison of $[C,N,O/Fe]$ of HD 179832(blue) with literature data (left) Data Source: Karinkuzhi et al. 2018; Merle 2016; Allen 2006; Barbuy 1992; Smith 1984. Comparison of heavy elements in HD 179832(green) with giants stars in literature (right) Data source: Luck and Heiter 2007(black); Swaelmen 2016(blue).

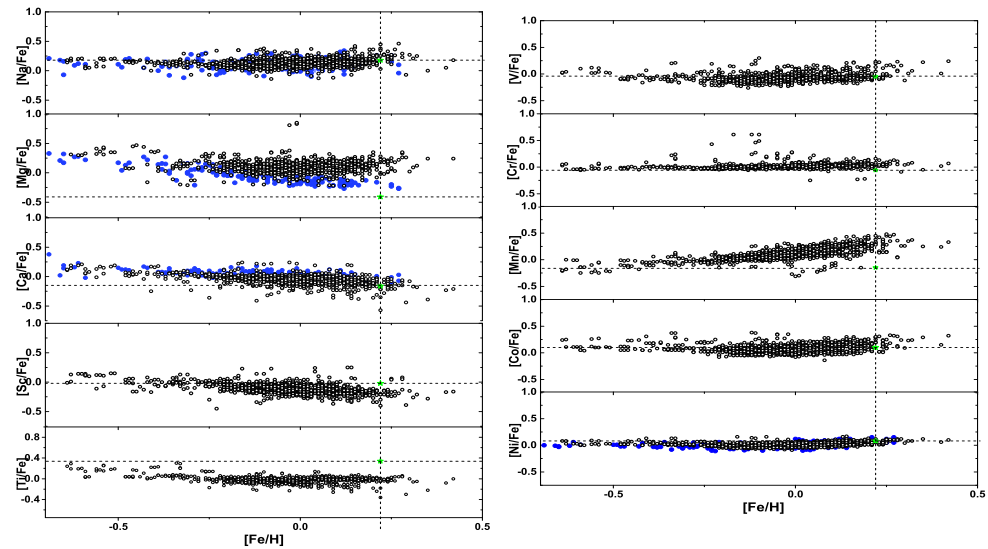


Figure 4.16: Comparison of light elements in HD 179832 (green) with giants stars in literature. Data source: Luck and Heiter 2007(black); Mishenina 2006(blue).

Element-wise conclusions

Carbon, Nitrogen and Oxygen: Carbon is found to lesser in Barium stars as we go to metal-rich sample as seen from Figure 4.15 (left). HD 179832 has the

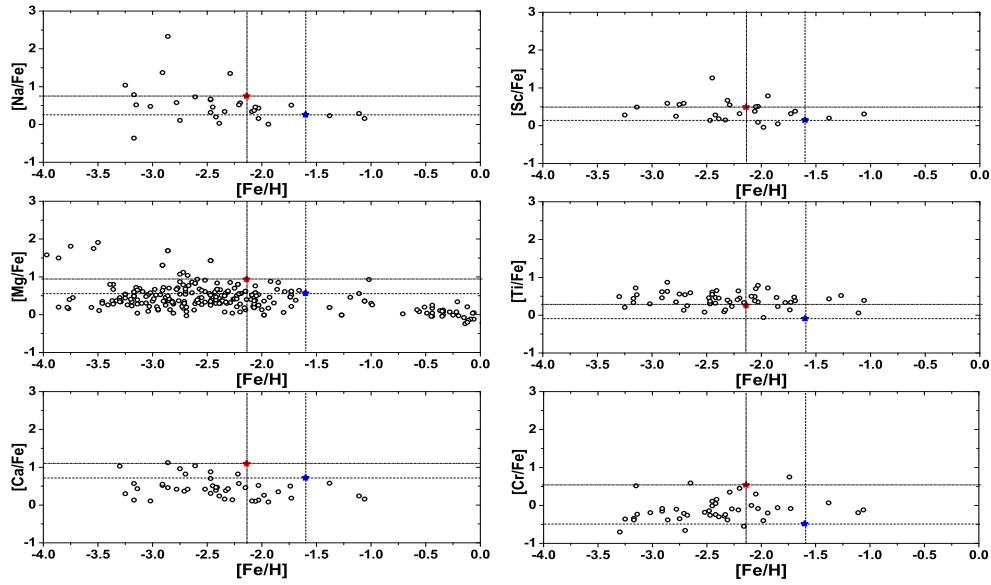


Figure 4.17: Comparison of light elements in HD 145777(red) and HE 2144-1832(blue) with CEMP stars in literature (black). Data source:Goswami et. al; 2006 Goswami et. al 2010; Goswami et. al 2016; Masseron 2010; Allen 2012; Aoki 2007; Barklem et al. 2005; Cohen et al. 2006

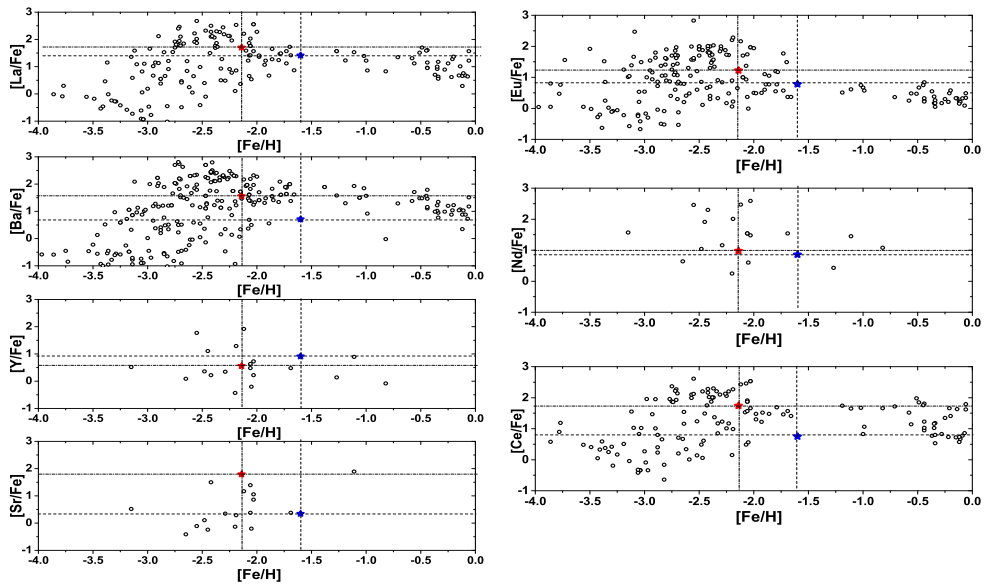


Figure 4.18: Comparison of heavy elements in HD 145777(red) and HE 2144-1832(blue) with CEMP stars in literature (black). Data source:Goswami et. al 2016; Masseron 2010; Allen 2012; Aoki 2007; Barklem et al. 2005; Cohen et al. 2006

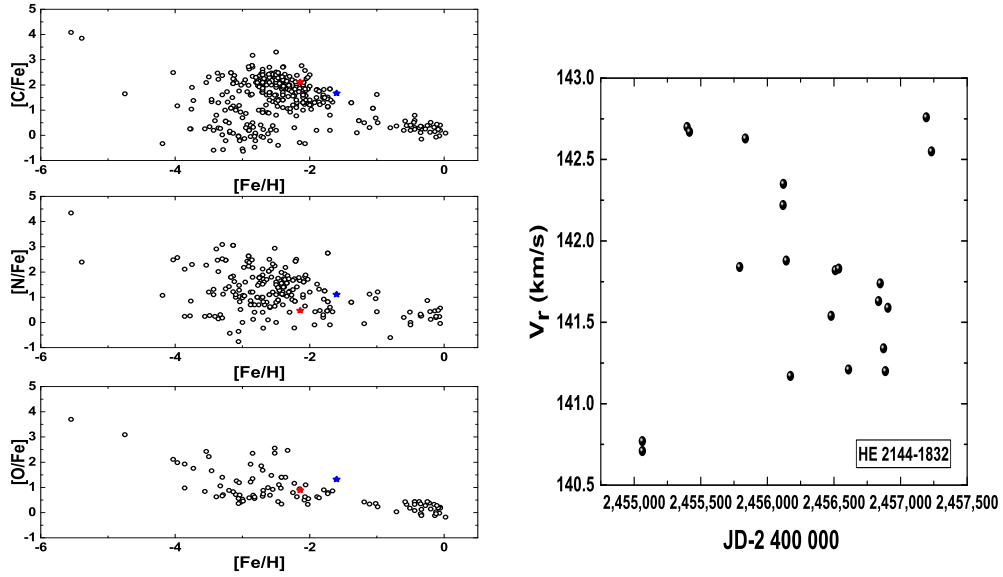


Figure 4.19: Comparison of [C,N,O/Fe] of HD 145777(red) and HE 2144-1832(blue) with literature data (left) Data Source: Masseron 2010; Allen 2012; Jonsell 2006; Abate 2015; Hansen 2016; Goswami 2006; Goswami 2016; Aoki 2007; Tsangarides 2005; Cohen et al. 2006. Radial velocity variations in HE 2144-1832 (right) Data Source: Jorissen et. al 2016;

least [C/Fe] being the most metal rich among the Barium star sample taken. Nitrogen has a similar trend with greater scatter than Carbon with stars as metal-poor as [Fe/H]=-0.5 having the same Nitrogen abundance as measured in our object. Oxygen is over-abundant than the majority of the sample and it clearly not following the trend. HD 145777 being more metal-poor than HE 2144-1832, has well observed trend of being more enhanced in carbon. However the story reverses in case of Nitrogen and Oxygen abundance. All three elements (C, N, O) do lie within the literature scatter.

Odd Z elements Na: Na abundance in HD 179832 seems to follow the trend for giants as seen in Figure 4.16 (left). The value lies very well within the small scatter. Whereas comparison with different subclasses of Barium stars, its [Na/Fe] value is very similar to weak Barium stars (See Figure 4.13 (left)). For the metal poor sample of programme stars, Na abundance of HE 2144-1832 fits tightly with the sample data at the nearby metallicity but HD 145777 abundances mimics the increasing scatter as the [Fe/H] goes -2.

α -elements Mg, Ca and Ti : Mg and Ca in HD 179832 clearly follow the decreasing trend in the literature values at metal-rich end. However in case of giants, the match is only with Ca. Mg is under-abundant. Ti does not follow either of the

trends in HD 179832 and is quite over-abundant as compared to the Barium sample taken. Mg has a marginal scatter around 0.5 in CEMP sample which is highly reflected by HE 2144-1832 whereas the other one lies at the upper end of the scatter being enhanced. The exact opposite is shown by Ti where HD 145777 is in sync with the literature framework but HE 2144-1832 is under-abundant. Increasing Ca abundance with lower metallicity is shown as well by these.

Iron-peak elements Mn and Ni: Manganese does follow the decreasing trend in HD 179832 and is consistent with the observational prediction. Ni shows the same behaviour of being within the tight scatter of both Normal giants as well as Barium sample.

Light s-process elements Sr, Y and Zr: Yttrium in HD 179832 shows near solar values validating the giants framework but is quite less in abundance values as compared to the Barium star sample taken. Probably this difference is due to mostly metal-poor Barium star sample of stars taken. In CEMP stars Yttrium and Strontium abundance is not available for large sample however the metallicity range is reasonable enough to make comparisons. Y has a maximum abundance scatter between -2 to -2.5 metallicity and HD 145777 lies right in the middle of it. HE 2144-1832 shows enhancements comparable to its more metal-poor counterparts.

Heavy s-process elements Ba, La, Eu: The Ba and La sample clearly shows a decreasing trend with increasing metallicity. HD 179832 furthers this observation whereas Eu abundances are almost the same as their metal-poor counterpart leading to a big scatter across metallicity. All three elements are enhanced compared to Normal giants. HE 2144-1832 agrees to the flat La trend around $[\text{Fe}/\text{H}] = -1.5$, whereas the scatter increases beyond this point encompassing $[\text{La}/\text{Fe}]$ of HD 145777 on its way. In Ba and Eu abundance also HD 145777 is part of the over-abundant population. HE 2144-1832 Ba abundance is slightly on the lower end as compared to local metallicity stars whereas Eu is in the middle of the scatter.

Heavy elements Nucleosynthesis efficiency Heavy elements nucleosynthesis is the ultimate signature of the neutron-processes which are or might have taken place in the star. There are couple of ways to infer that, each one giving an unique piece of information. Studies [9] have used stellar models and observations to construct the solar abundance database to a very significant level using photospheric and meteorite data. Even further studies [8] have used the correct models and values of neutron irradiation and nuclear reactions cross-sections to decouple the solar abundances in terms of their contribution from s-process and r-process. Such an information is very important and useful to get a handle over the origin of elemental abundances and further tracing down the dominating nuclear reaction contribution.

Figure 4.20 (left) shows solar [9] elemental abundances as a function of their atomic number (Z). It is clear from the distribution that Hydrogen and Helium are the most abundant species and the rest goes decreasing subsequently. We are mainly concerned with species $38 \leq Z \leq 90$. This range consists of three elements of key interest which gives the well known three peaks in the given abundance distribution. The first peak is of Strontium ($Z=38$), while the second and the third are Barium ($Z=56$) and Lead ($Z=82$). The first peak represents the efficiency of light s-process production whereas second peak represents the heavy s-process production rate. Lead, the third s-process peak is supposed to be a matter of debate a s-process nucleosynthesis result or radioactive decay of r-process products such as Thorium ($Z=90$) and Uranium ($Z=92$). Figure 4.20 (right) shows the solar [8] abundances with its composition broken down to s-process and r-process trends. Both these constituents separate out clearly at Europium ($Z=63$), forms the basis of r-process production indicator. After this element the r-process contribution to the total solar abundance of corresponding element takes over.

We use these two important information and in Figure 4.21 see the corresponding metallicity scaled observed abundances of programme stars against the solar values. The trend has been scaled to Barium peak. We can clearly see in all three plots the over-abundance of these neutron-capture elements showing the efficiency of nucleosynthesis in these stars with respect to solar.

Another perspective is to look at the ratio of heavy elements abundances to light elements abundances for s-process efficiency. We first find $[ls/Fe]$ which is taken for light s-process elements where $ls=(Y, Zr)$. Then we calculate the similarly for heavy s-process element ratio $[hs/Fe]$, where $hs=(La, Ce, Nd)$. The difference of these ratios will eventually give $[hs/ls]$ ratio which conveys s-process efficiency. A positive value of this ratio indicates higher production of heavier s-process elements and vice versa. These results are compiled in Table 4.17. We

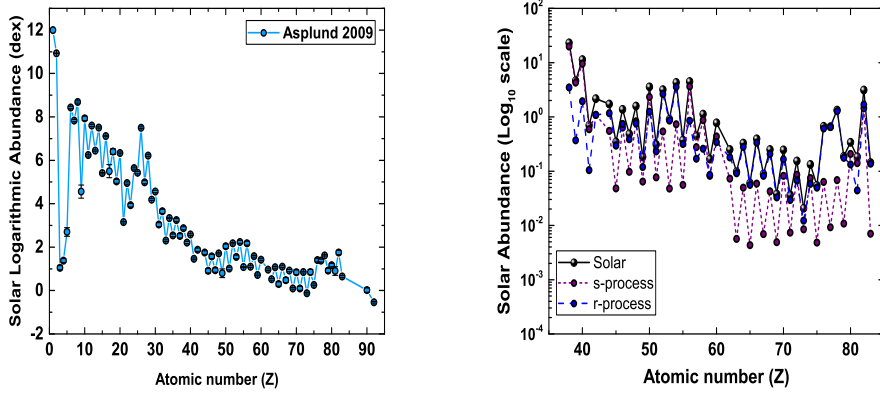


Figure 4.20: Solar elemental abundances from Asplund 2009(left). Contribution of the total solar composition(black) from s-process(purple) and r-process(blue)(right).

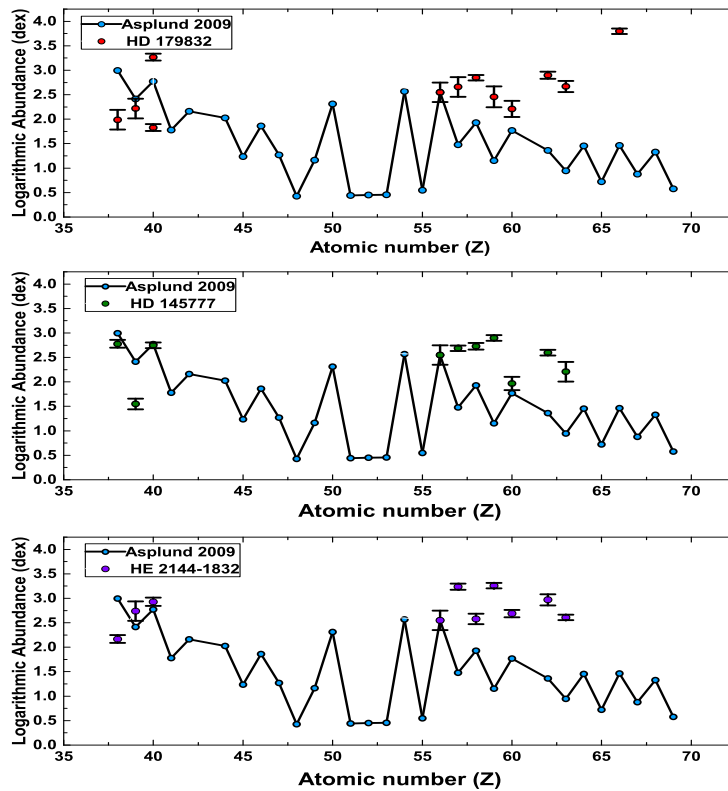


Figure 4.21: Comparison of heavy elements production in HD 179832(red); HD 145777(green) and HE 2144-1832(purple) compared to literature solar value(cyan).

notice that HD 179832 and HD 145777 have quite high and positive $[\text{hs}/\text{ls}]$ ratio where HE 2144-1832 has this ratio to be zero. Sr and Zr abundance used in the calculations are derived from line analysis because the synthesis could not be done with blended lines. So we expect $[\text{ls}/\text{Fe}]$ to be overestimated. This would imply the actual expected $[\text{hs}/\text{ls}]$ to be positive. This is very much expected at lower metallicities.

Table 4.17: Abundance ratios

Star Name	$[\text{ls}/\text{Fe}]$	$[\text{hs}/\text{Fe}]$	$[\text{hs}/\text{ls}]$
HD 179832	0.28	0.40	0.12
HD 145777	1.16	1.47	0.31
HE 2144-1832	1.01	1.01	0.00

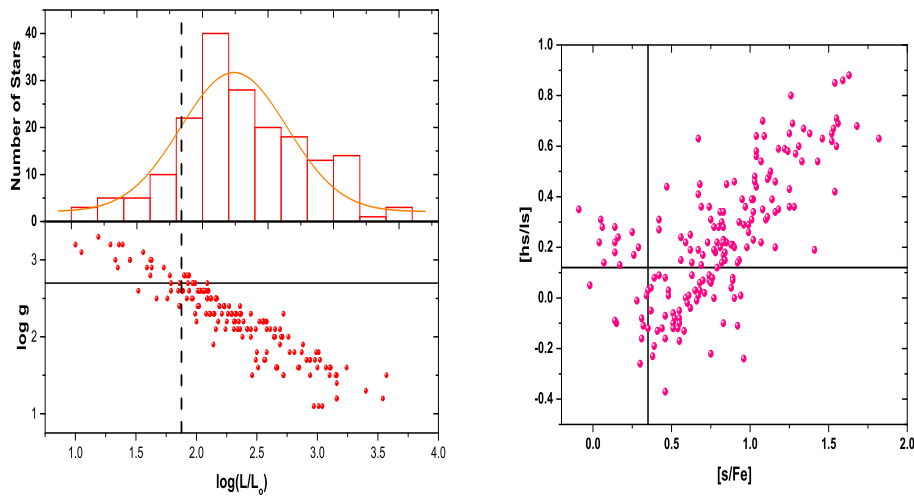


Figure 4.22: Surface gravity v/s Luminosity trend in HD179832 with literature (de Castro 2016) on the left. Heavy and light s-process elements ratio plotted with total s-process efficiency (right).

Figure 4.22 (right) shows the variation of $[\text{hs}/\text{ls}]$ ratio as a function of total s-process efficiency $[\text{s}/\text{Fe}]$ in a sample [27] of Barium stars compared with HD 179832. Here hs and ls are same as mentioned before whereas total s-process is represented by Y, Zr, La, Ce and Nd. It is very clear from plot that there is a positive correlation between s-process efficiency and $[\text{hs}/\text{ls}]$ ratio. The lines in the plot represent that of HD 179832, follow the same trend. One could infer the manifestation of this trend from Figure 4.23 (left) where both these parameters have a anti-correlation with metallicity. Although there are no samples with comparable $[\text{Fe}/\text{H}]$ but the trend could be well extrapolated. The topic of mean $[\text{s}/\text{Fe}]$ ratio is

still debatable for Barium stars. Studies have claimed it to be as low as 0.21 [78] and as high as ≥ 0.51 [70]. Since we have taken a homogeneous sample of de Castro [27] for comparison, we consider the minimum $[s/Fe]$ value for an object to be Barium star as 0.25. HD 179832 lies above this limit and clearly passes the s-process efficiency test for this category. Similarly, Figure 4.23 (right) concludes the anti-correlation trend in CEMP sample [1, 2] followed by HD 145777 and HE 2144-1832. Our values lie well within the scatter expected from the literature of CEMP stars. The scatter intrinsically is attributed to initial mass of the star along with metallicity. The number of thermal pulses taking place could significantly affect these values as well. This trend could be explained by the low metallicity corresponding to lesser seed nuclei giving rise to higher neutron to seed ratio. This in turn will result in greater efficiency of s-process element formation via neutron-capture processes. These $[s/Fe]$ and $[hs/ls]$ ratios have an intricate connection with the stellar processes happening within it. As de Castro [27] pointed out that higher ratios would also imply an efficient dredge-up. This is also indicated by high $[C/O]$ ratio which favours Carbon abundance when these convective processes via dredge-up, brings it from the deeper layers of the star to the surface. Thermally pulsating AGB is the most most efficient phase of dredge-ups, altering the surface chemical composition.

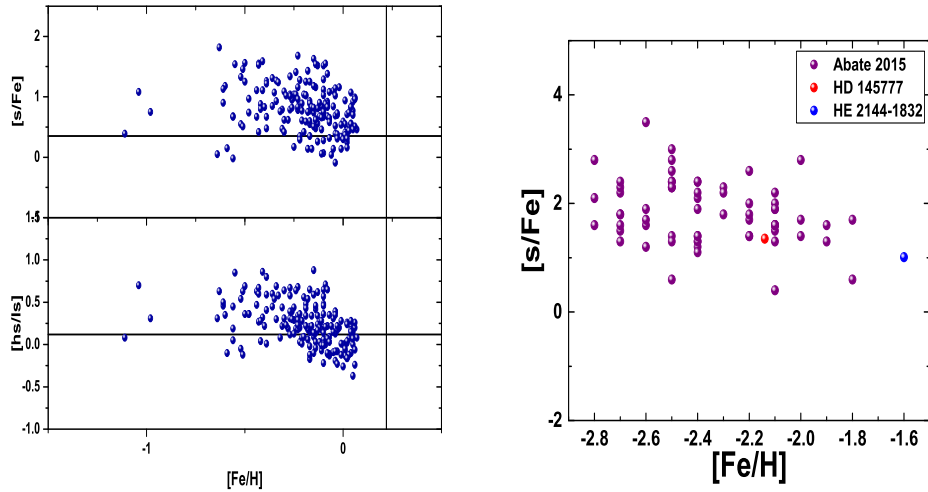


Figure 4.23: Heavy and light s-process elements ratio v/s metallicity trend in HD179832 with literature (de Castro 2016) on the left and for HD 145777(red); HE 2144-1832(blue) along with literature(purple) on the right.

Chapter 5

Conclusions

5.1 Existing Nucleosynthesis Theory

The site for production of both r-process and s-process elements are found to be different as per the neutron density. On one hand where s-process elements need neutron densities of around $10^6 - 10^{10} \text{ cm}^{-3}$ [20] which was attributed to AGB stars [48], the other one requires high neutron densities of $\approx 10^{20} \text{ cm}^{-3}$ [58] which could only be achieved in high mass star (Supernova) or compact binary mergers [83, 90]. But observation data was not conveying the same story as the low-mass stars did reveal enhancements in r-process elements as well. Apart from the scenarios suggested in subsection 2.2.1, the most promising framework is the treatment of intermediate neutron densities $10^{12} - 10^{15} \text{ cm}^{-3}$ [28, 39] explaining both types of yields from one single process.

Comparison with theoretical yields: We take i-process models yields of intermediate neutron density treatment computations [39] to compare with our results. These are yields[X/Fe] with neutron densities ranging from $10^{12} - 10^{15} \text{ cm}^{-3}$. As these are pure abundances coming out of a single layer of the star with no dilution or mixing, to compare with realistic scenarios they have to be normalized. We have adopted Ba abundance normalisation method where we fix the Barium abundance of all the yield to our observation results, since this is a robust peak to produce. Dilution can also be used by introducing a free parameter d . in the equation below:

$$X = X_i(1 - d) + X_{\odot}d \quad (5.1)$$

where X_i is the model yield and X_{\odot} is solar scaled abundance. We can see from Figure 5.1 that for HD 179832 $n = 10^{13} \text{ cm}^{-3}$ model fits the best whereas for HD 145777 $n = 10^{12} \text{ cm}^{-3}$ and $n = 10^{13} \text{ cm}^{-3}$ seems like the closest estimate. HE 2144-1832 is showing high abundances and could not be reproduced by any of the

models. However a key thing to note is that heavier elements are not estimated to good levels in both the plots (Figure 5.1) . This can be because of the physical inputs for those elements in the models or some overestimation of the observational data. The latter may not be the major factor here.

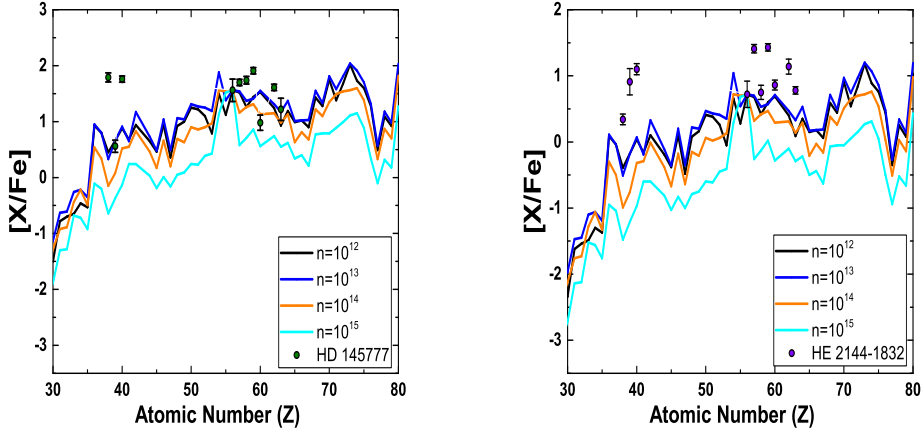


Figure 5.1: Comparison of our CEMP stars with i-process theoretical models

5.2 Object-wise conclusions

5.2.1 HD 179832

- From a detailed High-resolution spectroscopy analysis we finally conclude that the object HD179832 is a K-0III spectral type metal-rich giant Barium star with effective temperature 4780 K, surface gravity 2.7, micro-turbulent velocity 1.12 Km/s, and metallicity 0.22. Further classification studies [38] makes this object to fall within super metal-rich stars ($0.2 \leq [\text{Fe}/\text{H}] \leq 0.5$).
- The equivalent width analysis as well as the spectral synthesis methods gives the chemical abundances of light and heavy elements. These are compared with the existing literature data. Finally, our preliminary Ba II line strength analysis along with chemical abundance analysis reveals HD 179832 to be consistent within the framework of Barium stars with enhanced Barium and other heavy element abundances with $\text{C}/\text{O} < 1$.
- Fe-peak elements such as Co, Ni, Cu and Zn show mild over-abundance where as Cr and Mn are under-abundant. Heavy elements such as Ba, La

and Eu show enhancement in abundances with $[X=Fe] \geq 0.42$ (where $X=$ Ba,La,Eu). The derived $[hs/lr] = 0.12$, an indicator of heavy s-process elements have higher abundances than light s-process ones indicating the s-process efficiency. The abundances are also consistent with other observed Barium star literature sample.

- Negative value of $[La/Ce]=-0.33$, indicates the operation of $^{13}C(\alpha,n)^{16}O$ reaction to produce maximum free neutrons for the nucleosynthesis of s-process elements [33]. The $[La/Nd]$ ratio being positive classifies [91] it be a normal Barium star with no peculiar r-contributions.
- Kinematic analysis gives $V_{spa} < 85$ km/s which confirms it to be a thin disk star [23] and hence explains its metal-rich nature. The object has negative $[\alpha/Fe]=-0.07$, which also follows the disk abundance trend. The object has a $2.5 M_{\odot}$ mass and 5.012×10^2 Myr age. Studies [56, 65] have tried to constrain the mild Ba stars in mass range $2.5-4.5 M_{\odot}$ and strong Ba stars in $1-3 M_{\odot}$. This classification is ambiguous for our object but we can conclusively say by Mennessier et al. [65] classification that since the mass is outside the range $1-1.6 M_{\odot}$, HD 179832 is not a Ba dwarf. Bringing in the surface gravity classification as discussed in Allen et al. [4], for dwarf stars ($\log g \geq 3.7$); subgiants ($2.4 < \log g < 3.7$); giants ($\log g \leq 2.4$) we conclude it to be a subgiant Barium star. Also Figure 4.5 shows the object to be in First giant branch phase. Since heavier elements are produced in AGB phase mostly and our object is not evolved enough (as concluded from mass and age analysis in section 4.5), hence we conclude that the observed over-abundance is due to enrichment by an evolved companion (binary mass-transfer scenario) and HD 179832 could be a possible radial velocity variable.
- Theoretical models [21] compliments the s-process elements enhancements shown by high $[s/Fe]$ and $[hs/lr]$ values. This is an indicator of the efficient s-process production of the AGB star that has transferred its nucleosynthesis results onto the Barium star observed.

5.2.2 HD 145777

- This object belongs to the Very metal poor (VMP) class with $[\text{Fe}/\text{H}] < -2$. It has quite low surface gravity ($\log g = 0.4$) which is consistent with its high luminosity making it a part of bright-giant class stars.
- The over-abundance of Barium and Europium $[\text{Ba}/\text{Fe}] > 1$; $[\text{Eu}/\text{Fe}] > 1$ along with $0 < [\text{Ba}/\text{Fe}] < 0.5$ classifies the programme star to belong to CEMP-r/s subclass. This means the star shows enrichment in both r-process and s-process elements. However there has not been any conclusive theoretical study to explain the origin of such type of enhancements. Though intermediate neutron density ($\sim 10^{14}$) treatment known as i-process nucleosynthesis theory seems like a possible candidate to produce good levels of enrichment from both s and r-process elements.
- All α -elements such as Mg, Si, Ca and Ti show over-abundance with Mg, Ti and Ca showing near unity $[\text{X}/\text{Fe}]$ abundance ratios. The abundance obtained for Al and Si are extremely high and with high uncertainty as they are obtained from line analysis of single line each which could be affected by severe broadening.
- Heavy elements show high enhancements in elements such as Sr, Zr, La, Ce, Pr, Ba, Eu and Sm with $[\text{X}/\text{Fe}] \geq 1.0$. These ratios being above unity implies the high neutron densities at the which nucleosynthesis reactions are operating. The object being a VMP star having low metallicity is a major contributing factor.
- Negative value of $[\text{La}/\text{Ce}] = -0.04$, indicated the operation of $^{13}\text{C}(\alpha, n)^{16}\text{O}$ reaction. Availability of high neutrons densities from this reaction along with lower metallicity explains the enhancements of elements observed to some extent. These enhancements are again validated by high $[\text{s}/\text{Fe}]$ ratio being above 1.
- Our kinematic analysis suggests it to be a Population II halo object with high spatial velocity (~ 236 km/s) which points towards origin of its low metallicity. Population probability studies also confirm it to be a halo star with probability 0.94. The object is in sub-giant phase with age around 8×10^2 Myrs. However this estimate has a large uncertainty due to extremely large errors ($\sim 83\%$) in parallax values in the GAIA survey data.
- Theoretical AGB models [21, 82, 18] predict negative value for $[\text{La}/\text{Nd}]$ ratio in Very Metal-poor star population considering various neutron sources to explain CEMP-r/s enrichment origin. HD 145777 has $[\text{La}/\text{Nd}] = 0.72$

which makes it an outlier with respect to the theory and needs to be studied in detail.

5.2.3 HE 2144-1832

- The HESP observed third programme star of this project is a possible candidate of CEMP-s star population with $[C/Fe]>1$ and $[Ba/Fe]\approx 1$. Earlier, large sample survey studies [40] of very few elements of this object have also claimed it to be a CEMP-s star.
- The object has much cooler temperature (4260 K) as compared to earlier two objects, consistent with literature photometric temperature studies with $\Delta T < 80$ K.
- The kinematic analysis confirms it to be a thin thick disk star with probability 0.95 but this is heavily affected by yet again errors ($\sim 50\%$) in parallax value in Simbad database. But due to its high spatial velocity (~ 173 km/s) and metallicity $[Fe/H]=-1.60$, it is a valid candidate to be a halo population. The isochrones could not estimate its age because of the availability of interpolation of stellar evolutionary models at the observed metallicity.
- HE 2144-1832 does show positive value of $[La/Ce]=0.66$, but this could not possibly be the signature of the operation of $^{22}Ne(\alpha, n)^{25}Mg$ reaction as it should be between 0.2-0.4 [33]. Due to low temperatures and metallicity (Z), stellar evolutionary tracks could not estimate the mass of the object which could have been a good alternative of the tracing the reaction providing the neutron source.
- However those stellar evolutionary tracks could very well give an idea of the object just transitioning from sub-giant to enter the first giant-branch phase. As a similar case in HD 179832, the heavy elements observed could not be explained alone without the binary AGB companion picture. To solve this puzzle, studies [46, 47] have established HE 2144-1832 to be a radial velocity variable (See Figure 4.19 (right)) which makes it a clear candidate to fall within the domain of AGB binary companion mass transfer scenario explaining its observed heavy elements.

References

1. Abate, C., Pols, O. R., Izzard, R. G., & Karakas, A. I. 2015a, A&A, 581, A22
2. Abate, C., Pols, O. R., Karakas, A. I., & Izzard, R. G. 2015b, A&A, 576, A118
3. Aoki W., Beers T. C., Christlieb N., Norris J. E., Ryan S. G., Tsangarides S., 2007, ApJ, 655, 492
4. Allen D. M., Barbuy B., 2006a, A&A, 454, 895
5. Allen, D. M., Ryan, S. G., Rossi, S., Beers, T. C., & Tsangarides, S. A. 2012, A&A, 548, A34
6. Alonso A., Arribas S., Martinez-Roger C., 1999, A&AS, 140, 261
7. Antipova, L.I., Boyarchuk, A.A., Pakhomov, Yu. V. & Panchuk, V.E., 2004, ARep, 48, 597
8. Arlandini, C., Kappeler, F., Wisshak, K., Gallino, R., Lugaro, M., Busso, M., & Straniero, O. 1999, ApJ, 525, 886
9. Asplund M., Grevesse N., Sauval A.J. & Scott P., 2009, ARA&A, 47, 481
10. Barbuy B., Jorissen A., Rossi S. C. F., Arnould M., 1992, A&A, 262, 216
11. Barklem, P. S., Christlieb, N., Beers, T. C., et al. 2005, A&A, 439, 129
12. Bartkevicius A., 1996, Balt. Astron., 5, 217
13. Beers T.C. & Christlieb N., 2005, ARA&A, 43, 531
14. Bensby, T., Feltzing, S., & Lundström, I. 2003, A&A, 410, 527
15. Betsy T., Feltzing S., Lundstrom I., 2004, A&A, 415, 155

16. Bidelman, W.P. & Keenan, P.C., 1951, ApJ, 114, 473
17. Bisterzo, S., Gallino, R., Straniero, O., Cristallo, S., Kppeler, F. 2011, MNRAS, 418, 284
18. Bisterzo, S., Gallino, R., Straniero, O, Cristallo, S., & K Ĺappeler, F. 2010,MNRAS, 404,1529
19. Burbidge E.M., Burbidge G.R., Foeler W.A. & Hoyle F., 1957, RvMP, 29, 547
20. Busso, M., Gallino, R., & Wasserburg, G. J. 1999, ARA&A, 37, 239
21. Busso, M., Gallino, R., Lambert, D. L., Travaglio, C., & Smith, V. V. 2001, ApJ,557, 802
22. Carollo, D., Freeman, K., Beers, T. C., et al. 2014, ApJ, 788, 180
23. Chen, B., Vergely, J.L, Valette, B. & Carraro, G., 1998, A&A, 336,137
24. Clayton, D. D. 1983, ApJ, 271, L107
25. Cohen, J. G., Christlieb, N., Qian, Y.-Z., Wasserburg, G. J. 2003, ApJ, 588, 1082557, 802
26. Cram, L. 1999, Trans. IAU XXIIIIB, ed. J. Andersen, p. 141
27. de Castro D.B., Pereira C.B., Roig F., Jilinski E., Drake N.A., Chavero C., Silva J.V., 2016, MNRAS, 459, 4299
28. Dardelet, L., Ritter, C., Prado, P., et al. 2015, arXiv:1505.05500
29. Drake, N. A., & Pereira, C. B. 2008, AJ, 135, 1070
30. Frebel, A., Christlieb, N., Norris, J. E., Aoki, W., Asplund, M. 2006, ApJL, 638, L17
31. Girardi L., Bressan A., Bertelli G., Chiosi C., 2000, A&AS, 141, 371
32. Gontcharov G. A., 2006, Astronomy Letters, 32, 759
33. Goriely, S., & Siess, L. 2005, IAU, 228, 451
34. Goswami A., 2005, MNRAS, 359, 531
35. Goswami, A., Aoki, W., Beers, T. C., et al. 2006, MNRAS, 372, 343

36. Goswami A., Aoki W., 2010, MNRAS, 404, 253
37. Goswami A., Aoki W. & Karinkuzhi D., 2016, MNRAS, 455, 402
38. Grenon, M. 1972, in Age des Etoiles, ed. G. Cayrel de Strobel, & A. M. Delplace, IAU Colloq., 17, 55
39. Hampel, M., Stancliffe, R. J., Lugaro, M., & Meyer, B. S. 2016, arXiv:1608.08634
40. Hansen, T. T., Andersen, J., Nordström, B., et al. 2016, A&A, 588, A3
41. Iben, I. 1975, ApJ, 196, 525 NASA ADS
42. Iben I., Renzini A., 1983, ARA&A 21, 271 (IR) NASA ADS
43. Johnson, D.R.H. & Soderblom, D.R., 1987, AJ, 93,864
44. Jonsell K., Barklem P.S., Gustafsson B., Christlieb N., Hill V., Beers T.C., Holmberg J., 2006, A&A, 451, 651
45. Jorissen, A., Van Eck S., Mayor, M., & Udry, S. 1998, A&A, 332, 877
46. Jorissen, A., Hansen, T., Van Eck, S., et al. 2016a, A&A, 586, A159
47. Jorissen, A., Van Eck, S., Van Winkel, H., et al. 2016b, A&A, 586, A158
48. Karakas, A. I. & Lattanzio, J. C. 2014, PASA, 31, 30
49. Karinkuzhi, D., Goswami, A., & Masseron, T. (2017). The Astrophysical Journal, 834(1), 61.
50. Karinkuzhi, Drisya, Aruna Goswami, Navin Sridhar, Thomas Masseron, and Meenakshi Purandardas, 2018, MNRAS
51. Kurucz R. L., 1991, Bulletin of the American Astronomical Society Vol. 23 of Bulletin of the American Astronomical Society, A New Theoretical Model Photosphere. p. 1047
52. Kurucz R. L., 1993, Dworetzky M. M., Castelli F., Faraggiana R., eds, IAU Colloq. 138: Peculiar versus Normal Phenomena in A-type and Related Stars Vol. 44 of Astronomical Society of the Pacific Conference Series, A New Opacity-Sampling Model Atmosphere Program for Arbitrary Abundances. p. 87

53. Kurucz R.L., 1995a, Adelman S.J., Wiese W.L., eds, ASP Conf. Ser. Vol. 78, Astrophysical Application of Powerful New Database. Astron. Soc. Pac., San Francisco, p. 205
54. Kurucz R.L., 1995b, Sauval A.J., Blomme R., Grevesse N., eds, ASP Conf. Ser. Vol. 81, Laboratory and Astronomical High Resolution Spectra. Astron. Soc. Pac., San Francisco, p. 583
55. Liang, Y. C., Zhao, G., Chen, Y. Q., Qiu, H. M., & Zhang, B. 2003, A&A, 397, 257
56. Lu, P.K., 1991, AJ, 101, 2229
57. Luck., R.E. & Heiter, U., 2007, AJ, 133, 2464
58. Lugaro, M. 2005, Stardust from Meteorites: An Introduction to Presolar Grains, World Scientific series in astronomy and astrophysics (World Scientific)
59. Lucatello, S., Tsangarides, S., Beers, T. C., et al. 2005, ApJ, 625, 825
60. Mahanta U. et al. (2016) MNRAS 463.2 : 1213-1223.
61. Masseron T., Plez B., Primas F., Van Eck S. & Jorissen, 2006, arXiv:astro-ph/0601253v1
62. Masseron T., Johnson J.A., Plez B., Van Eck S., Primas F., Goriely S. & Jorissen A., 2010, A&A, 509, A93
63. McClure R. D., Fletcher J. M. & Nemej J., 1980, ApJ, 238, L35
64. McClure R. D., Woodsworth A. W., 1990, ApJ, 352, 709
65. Mennessier, M. O., Luri, X., Figueras, F. et al. 1997, A&A, 326, 722
66. Merle, T., Jorissen, A., Van Eck, S., Masseron, T., Van Winckel, H., 2016, A&A, 586, 151
67. Mishenina, T. V., Soubiran, C., Kovtyukh, V. V., & Korotin, S. A. 2004, A&A, 418, 551
68. Mishenina, T.V., Bienayme, O., Gorbaneva, T.I., Charbonnel, C., 2006, AA, 456, 1109
69. Pereira, C.B. & Drake, N.A., 2009, A&A, 496, 791

70. Pilachowski, C.A., 1977, A&A, 54, 465
71. Qian, Y.-Z., Wasserburg, G. J. 2003, ApJ, 588, 1099
72. Reddy, B.E., Lambert, D.L. & Allende Prieto, C., 2006, MNRAS, 367,1329
73. Refsdal, S., & Weigert, A. 1971, AA, 13, 367 Astrophysics, 56, 57
74. Rossi S., Beers T. C., Sneden C., 1999, in Gibson B. K., Axelrod T. S., Putman M. E., eds, ASP Conf Ser. Vol. 165, The Third Stromlo Symposium: the Galactic Halo. Astron. Soc. Pac., San Francisco, p. 264
75. Sanders, R. H. 1967, Ap. J., 150, 971.
76. Smith V. V., 1984, A&A, 132, 326
77. Sneden, C., 1973, Ph.D. Thesis, Univ. of Texas
78. Sneden, C., Lambert, D.L. Pilachowski, C.A., 1981, ApJ, 247, 1052
79. Schonrich, R., Binney, J. & Dehnen, W., 2010, MNRAS, 403,1829
80. Smith V.V., Coleman H. & Lambert D.L., 1993, ApJ, 417, 287
81. Schwarzschild M., Härm R., 1967, ApJ, 150, 961
82. Straniero, O., Gallino, R., & Cristallo, S. 2006, Nucl. Phys. A, 777, 311
83. Thielemann, F.-K., Arcones, A., Käppeli, R., Liebendörfer, M., Rauscher, T., Winteler, C., Fröhlich, C., Dillmann, I., Fischer, T., Martinez-Pinedo, G., Langanke, K., Farouqi, K., Kratz, K.-L., Panov, I., & Korneev, I. K. 2011, Progress in Particle and Nuclear Physics, 66, 346
84. Tsangarides S. A., 2005, PhD thesis, Open University (United Kingdom), England
85. Van der Swaelmen, M., Barbuy, B., Hill, V., et al. 2016, A&A, 586, A1
86. Vanture A. D., 1992b, AJ, 104, 1986
87. Yang G., Liang Y., Spite M., Chen Y., Zhao G., Zhang B., Liu G., Liu Y., Liu N., Deng L., Spite F., Hill V., Zhang C., 2016, RAA, 16, 19
88. Wallerstein G., Knapp G., 1998, ARA&A, 36, 369
89. Wanajo, S., Nomoto, K., Iwamoto, N., Ishimaru, Y., Beers, T. C. 2006, ApJ, 636, 842

90. Wehmeyer, B., Pignatari, M., & Thielemann, F.-K. 2015, MNRAS, 452, 1970
91. W. Y. Cui, B. Zhang, J. R. Shi, G. Zhao, W. J. Wang, P. Niu, 2014, arXiv:1405.4185v1
92. Zijlstra, A. A. 2004, MNRAS, 348, L23
93. Aruna Goswami & E. Reddy, Principles and Perspectives in Cosmochemistry, Springer

Appendix A

A.1 Python Codes

A.1.1 Photometric Estimate

```
print("#-----Give inPuts -----#")
J=input(" enter J=")
H=input(" enter H=")
K=input(" enter K=")
B=input(" enter B=")
V=input(" enter V=")
M=input(" enter M=")

print("----- start calculations -----")
Jtcs=J+0.001-0.049*(J-K)
Htcs=H-0.018+0.003*(J-K)
Ktcs=K-0.014+0.034*(J-K)
#Print JT
#Print KT
#-----
Kj=Ktcs+0.042-0.019*(((Jtcs-Ktcs)-0.008)/0.910)
VKtcs=0.050+0.993*(V-Kj)
#-----
Tjk=0.582+(0.799+0.085*(Jtcs-Ktcs))*(Jtcs-Ktcs)
Tjh=0.587+(0.922+0.218*(Jtcs-Htcs)+0.016*M)*(Jtcs-Htcs)
Tvk=0.555+(0.195+0.013*VKtcs-0.008*M)*VKtcs+(0.009-0.002*M)*M
Tbv=0.541+(0.533+0.007*(B-V)-0.019*M)*(B-V)-(0.047+0.011*M)*M

#-----
print "T_EFF_JK=",5040/Tjk
```

```

print "T_EFF_JH=",5040/Tjh
print "T_EFF_VK=",5040/Tvk
print "T_EFF_BV=",5040/Tbv
print "done"

```

A.1.2 Kinematic Analysis

```

###-----matrix definition-----###
import numpy as np          # module for matrix
from math import*          #module for math

#-----taking input-----##
print ("-----Give the inputs-----")
a=input("input alpha=")
d=input("input delta=")
V_r=input(" V_r=")
k=input("k=")
mu1=input(" mu_alpha=")
mu2=input(" mu_delta=")
p=input("Put parallax=")
print("----- calculating -----")

#----matrix definitions-----#
T= np. array ([[ -0.06699, -0.87276, -0.48354],[0.49273, -0.45035,0.7445
[ -0.86760, -0.18837,0.46020]])
##define T
A=np. array ([[ cos(a)*cos(d), - sin(a), - cos(a)* sin(d) ] ,
[ sin(a)*cos(d), cos(a), - sin(a)* sin(d) ] , [ sin(d) ,0.0 , cos(d) ]])
#define A
u=np. zeros (shape =(3 ,1))
c=np. array ([[ V_r ] ,[(k*mu1)/p] ,[(k*mu2)/p]])
print("----- start -----")
print "T=",T
print "A=",A

##-----B=T.A-----##
B=np. zeros (shape =(3 ,3))          ## making (3,3) null matrix
for i in range(3):

```

```

for j in range(3):
for k in range(3):
B[i][j]=B[i][j]+T[i][k]*A[k][j]
##-----matrix multiplication
print "B=",B

##-----final solution-----##
for i in range(3):
for j in range(1):
for k in range(3):
u[i][j]=u[i][j]+B[i][k]*c[k][j]
print "u=",u
##-----solution----##
print("-----solution-----")

u1=11.1+u[0][0]
v1=12.2+u[1][0]
w1=7.3+u[2][0]
print "u=",u1
print "v=",v1
print "w=",w1
sp=(u1**2)+(v1**2)+(w1**2)
print "spatial velocity=",sqrt(sp)
print("-----error calculation-----")
e_vr=input("e_vr=")
e_p=input("e_p=")
e_mu1=input("e_mu_alpha=")
e_mu2=input("e_mu_delta=")
k=1
E=np.array([[e_vr**2],[((k/p)**2)*((e_mu1**2)+((mu1*e_p/p)**2))],
[[((k/p)**2)*((e_mu2**2)+((mu2*e_p/p)**2))]])
print ("error matrix="),E

```

A.2 Line-lists

Table A.1: Element Line-list HD 179832

Wavelength (Å)	Element	E.P. low (eV)	log (gf)	Equivalent width (mÅ)
4489.739	Fe I	0.121	-3.966	180.2
4939.687		0.859	-3.340	173.2
5054.643		3.640	-2.140	75.71
5090.773		4.256	-0.400	121.0
5141.739		2.424	-2.150	142.4
5198.711		2.223	-2.135	167.4
5215.180		3.266	-0.967	164.4
5217.389		3.211	-1.162	144.9
5285.127		4.435	-1.640	55.35
5307.361		1.608	-2.987	153.7
5321.108		4.435	-1.440	71.93
5322.041		2.279	-3.030	113.0
5373.709		4.473	-0.860	86.53
5379.574		3.695	-1.480	101.5
5389.479		4.415	-0.410	109.5
5398.279		4.446	-0.670	96.85
5441.339		4.312	-1.730	62.65
5466.396		4.371	-0.630	106.1
5522.446		4.209	-1.550	76.08
5576.089		3.430	-1.000	142.5
5679.024		4.652	-0.920	81.10
5686.530		4.548	-0.630	105.1
5775.081		4.220	-1.298	90.53
5793.915		4.220	-1.700	65.17
5806.726		4.608	-1.050	82.86
5855.076		4.608	-1.760	46.96
5883.817		3.960	-1.360	101.3
5916.247		2.453	-2.994	110.6
5930.181		4.652	-0.230	113.0
5934.655		3.929	-1.170	105.3
5956.694		0.859	-4.605	126.5
6003.011		3.882	-1.120	113.9
6027.051		4.076	-1.210	93.96
6056.005		4.733	-0.460	92.99
6078.491		4.795	-0.481	100.1
6079.008		4.652	-1.120	68.59
6151.617		2.176	-3.299	105.7
6165.360		4.143	-1.550	78.96

Table A.2: Fe Line-list HD 179832 continuing

Wavelength (Å)	Element	E.P. low (eV)	log (gf)	Equivalent width (mÅ)
6173.334		2.223	-2.880	125.9
6187.989		3.943	-1.720	85.83
6200.313		2.608	-2.437	125.9
6213.430		2.223	-2.660	143.8
6219.281		2.198	-2.433	152.4
6229.226		2.845	-2.970	91.96
6232.640		3.654	-1.200	120.6
6315.811		4.076	-1.710	81.03
6322.685		2.588	-2.426	132.2
6335.330		2.198	-2.230	161.4
6411.648		3.654	-0.820	150.1
6419.949		4.733	-0.240	107.5
6546.238		2.759	-1.650	160.6
6569.214		4.733	-0.420	102.6
6593.870		2.433	-2.422	141.7
6597.559		4.795	-1.070	66.31
6608.025		2.279	-4.030	73.40
6609.110		2.559	-2.692	118.5
6627.544		4.548	-1.680	56.46
6733.150		4.638	-1.580	51.75
6750.152		2.424	-2.621	130.3
6810.262		4.607	-1.120	76.59
6843.655		4.548	-0.930	96.30
6858.148		4.608	-1.060	74.48
7071.860		4.607	-1.700	52.27
7219.682		4.076	-1.690	80.35
4620.521	Fe II	2.828	-3.280	76.18
4993.358		2.807	-3.650	61.74
5234.625		3.221	-2.050	104.6
5414.073		3.221	-3.790	40.16
5425.257		3.199	-3.360	58.12
5991.376		3.153	-3.557	49.21
6149.258		3.889	-2.724	44.39
6247.557		3.892	-2.329	67.54
6456.383		3.903	-2.075	78.40

Table A.3: Element Line-list HD 179832

Wavelength (Å)	Element	E.P. low (eV)	log (gf)	Equivalent width (mÅ)
6300.304	O I	0.000	-9.819	35.07
7771.944	O I	9.146	0.324	40.88
7774.166	O I	9.146	0.174	43.92
7775.388	O I	9.146	-0.046	38.45
5682.633	Na I	2.102	-0.700	149.7
5688.203	Na I	2.105	-0.450	149.4
6318.705	Mg I	5.108	-1.730	67.16
4782.991	Si I	4.954	-2.470	29.62
6414.980	Si I	5.871	-1.100	50.90
5793.073	Si I	4.930	-2.060	62.34
6555.463	Si I	5.984	-1.000	45.28
4578.560	Ca I	2.521	-0.560	132.2
5512.975	Ca I	2.933	-0.290	113.6
5581.963	Ca I	2.523	-0.710	131.2
5588.748	Ca I	2.526	-0.210	174.6
5590.111	Ca I	2.521	-0.710	124.9
6449.801	Ca I	2.521	-0.550	140.0
6455.592	Ca I	2.523	-1.350	105.8
6471.648	Ca I	2.526	-0.590	133.8
6493.772	Ca I	2.521	-0.140	161.8
6499.639	Ca I	2.523	-0.590	128.1
6245.607	Sc II	1.507	-0.980	82.88
4820.399	Ti I	1.502	-0.441	118.1
4820.399	Ti I	1.502	-0.441	118.1
4453.312	Ti I	1.430	-0.051	120.0
4453.711	Ti I	1.873	-0.010	114.0
5087.047	Ti I	1.430	-0.780	109.9
4937.727	Ti I	0.813	-2.254	70.59
5064.650	Ti I	0.047	-0.991	171.7
4470.856	Ti II	1.165	-2.280	106.3
4568.337	Ti II	1.224	-2.650	84.26
4657.205	Ti II	1.243	-2.150	101.9
5185.902	Ti II	1.893	-1.350	105.9
5727.038	V I	1.081	-0.012	122.7
5727.652	V I	1.051	-0.870	63.47
6531.406	V I	1.218	-0.840	47.19
4652.171	Cr I	1.004	-1.030	167.1
5247.565	Cr I	0.961	-1.640	142.7

Table A.4: Element Line-list HD 179832 continuing

Wavelength (Å)	Element	E.P. low (eV)	log (gf)	Equivalent width (mÅ)
5348.317	Cr I	1.004	-1.290	164.3
4588.199	Cr II	4.071	-0.630	81.64
4592.050	Cr II	4.073	-1.220	61.77
4451.592	Mn I	2.888	0.278	141.1
4761.522	Mn I	2.953	-0.138	120.6
4765.860	Mn I	2.941	-0.080	116.0
4781.429	Co I	1.882	-2.150	59.72
4792.853	Co I	3.252	-0.067	70.78
4813.467	Co I	3.216	0.050	93.32
5530.775	Co I	1.710	-2.060	87.62
5590.739	Co I	2.042	-1.870	70.91
6454.990	Co I	3.632	-0.250	48.56
6632.424	Co I	2.280	-2.000	47.68
4470.488	Ni I	3.399	-0.310	106.2
4814.593	Ni I	3.597	-1.620	47.98
4852.554	Ni I	3.542	-1.070	76.50
4937.338	Ni I	3.606	-0.390	118.7
4953.201	Ni I	3.740	-0.580	96.41
5035.363	Ni I	3.635	0.290	123.3
5081.111	Ni I	3.847	0.290	129.3
5082.344	Ni I	3.658	-0.540	99.44
5084.096	Ni I	3.678	0.030	107.3
5099.927	Ni I	3.678	-0.100	102.7
5102.966	Ni I	1.676	-2.620	115.4
6086.269	Ni I	4.266	-0.530	64.58
6111.060	Ni I	4.088	-0.870	62.57
4722.161	Zn I	4.030	-0.338	93.19
4810.533	Zn I	4.078	-0.137	90.57
4607.334	Sr I	0.000	-0.570	100.8
4854.867	Y II	0.992	-0.380	92.08
5087.418	Y II	1.080	-0.170	85.55
5119.113	Y II	0.992	-1.360	53.04
5289.816	Y II	1.033	-1.850	26.44
5544.608	Y II	1.738	-1.090	29.05
4739.480	Zr I	0.651	0.230	53.01
4772.323	Zr I	0.623	0.040	40.47
6134.585	Zr I	0.000	-1.280	24.73
4414.539	Zr II	1.236	-1.111	75.66

Table A.5: Element Line-list HD 179832 continuing

Wavelength (Å)	Element	E.P. low (eV)	log (gf)	Equivalent width (mÅ)
5853.678	Ba II	0.604	-1.000	120.2
6496.898	Ba II	0.604	-0.377	169.8
4628.167	La II	0.516	0.008	75.10
4748.733	La II	0.927	-0.860	24.34
5274.227	La II	1.044	-0.323	40.48
4562.359	Ce II	0.478	0.081	76.82
5219.040	Pr II	0.795	-0.240	23.73
5259.725	Pr II	0.633	0.080	27.64
4446.384	Nd II	0.205	-0.590	69.92
4947.031	Nd II	0.559	-1.250	15.63
4961.392	Nd II	0.631	-0.710	28.21
5089.837	Nd II	0.205	-1.160	25.40
5276.869	Nd II	0.859	-0.440	19.04
5319.805	Nd II	0.550	-0.210	73.00
4499.470	Sm II	0.248	-1.413	33.29
4519.630	Sm II	0.544	-0.751	37.94
4566.218	Sm II	0.333	-1.245	38.15
4577.692	Sm II	0.248	-1.234	41.88
4791.579	Sm II	0.104	-1.846	25.67
6437.647	Eu II	1.320	-0.276	23.15
6645.090	Eu II	1.380	-0.204	30.45
4923.159	Dy II	0.103	-2.384	44.90

Table A.6: Fe Line-list HD 145777

Wavelength (Å)	Element	E.P. low (eV)	log (gf)	Equivalent width (mÅ)
4632.911	Fe I	1.608	-2.913	72.40
4871.318		2.865	-0.410	136.3
4924.770		2.279	-2.220	68.64
5028.126		3.573	-1.123	21.61
5079.223		2.198	-2.067	82.33
5242.491		3.634	-0.840	42.98
5266.555		2.998	-0.490	130.4
5283.621		3.241	-0.630	106.2
5339.929		3.266	-0.680	87.39
5364.871		4.446	0.220	58.35
5367.466		4.415	0.350	69.25
5586.756		3.368	-0.210	121.0
6136.615		2.453	-1.400	133.8
6137.691		2.588	-1.403	117.0
6230.722		2.559	-1.281	121.7
6301.500		3.654	-0.672	65.34
5534.847	Fe II	3.245	-2.930	28.00
6247.557		3.892	-2.329	30.16
6456.383		3.903	-2.075	32.16

Table A.7: Element Line-list HD 145777

Wavelength (Å)	Element	E.P. low (eV)	log (gf)	Equivalent width (mÅ)
6300.304	O I	0.000	-9.819	31.38
7771.944	O I	9.146	0.324	15.93
7774.166	O I	9.146	0.174	83.00
7775.388	O I	9.146	-0.046	62.71
5682.633	Na I	2.102	-0.700	33.20
5688.203	Na I	2.105	-0.450	37.58
5528.405	Mg I	4.346	-0.620	136.5
6783.638	Al I	4.021	-1.440	70.51
6555.463	Si I	5.984	-1.000	107.7
5261.704	Ca I	2.521	-0.730	64.83
5588.749	Ca I	2.526	-0.210	102.6
5590.114	Ca I	2.521	-0.710	67.34
5594.462	Ca I	2.523	-0.050	92.58
6449.808	Ca I	2.521	-0.550	112.4
6493.781	Ca I	2.521	0.140	157.2
6499.650	Ca I	2.523	-0.590	98.14
6245.637	Sc II	1.507	-0.980	120.9
4840.879	Ti I	0.899	-0.509	84.13
4999.503	Ti I	0.826	0.250	141.1
5185.913	Ti II	1.893	-1.350	99.52
4626.173	Cr I	0.968	-1.320	75.54
5247.565	Cr I	0.961	-1.640	76.67
5348.315	Cr I	1.004	-1.290	86.41
4766.418	Mn I	2.920	0.100	35.39
4792.846	Co I	3.252	-0.067	30.93
4852.547	Ni I	3.542	-1.070	54.78
4937.341	Ni I	3.606	-0.390	110.2
5035.357	Ni I	3.635	0.290	83.78
5084.089	Ni I	3.678	0.030	55.01
4722.153	Zn I	4.030	-0.338	56.49
4810.528	Zn I	4.078	-0.137	58.07
4607.327	Sr I	0.000	-0.570	51.79
4854.863	Y II	0.992	-0.380	93.22
5087.416	Y II	1.084	-0.170	116.8
5662.925	Y II	1.944	0.160	82.90
4739.480	Zr I	0.651	0.230	26.43

Table A.8: Element Line-list HD 145777 continuing

Wavelength (Å)	Element	E.P. low (eV)	log (gf)	Equivalent width (mÅ)
4748.726	La II	0.927	-0.860	59.10
4628.161	Ce II	0.516	0.008	127.2
5274.229	Ce II	1.044	-0.323	82.62
5330.556	Ce II	0.869	-0.760	57.94
5322.772	Pr II	0.483	-0.315	90.16
4947.020	Nd II	0.559	-1.250	28.85
4961.387	Nd II	0.631	-0.710	84.30
5276.869	Nd II	0.859	-0.440	44.51
5319.815	Nd II	0.550	-0.210	107.4
4791.580	Sm II	0.104	-1.846	28.60
6437.640	Eu II	1.320	-0.276	40.77
6645.090	Eu II	1.380	-0.204	49.01

Table A.9: Line-list of HE 2144-1832

Wavelength (Å)	Element	E.P. low (eV)	log (gf)	Equivalent width (mÅ)
4445.471	Fe I	0.087	-5.441	112.0
4446.833		3.686	-1.330	65.68
4630.121		2.279	-2.600	97.07
4882.144		3.417	-1.640	64.44
5028.126		3.573	-1.474	73.36
5247.049		0.087	-4.946	162.2
5253.461		3.283	-1.670	92.64
5281.790		3.039	-1.020	137.6
5322.041		2.279	-3.030	83.71
5339.928		3.626	-0.680	122.8
5586.756		3.368	-0.210	158.5
5638.262		4.220	-0.870	66.56
5753.121		4.260	-0.760	62.58
5976.775		3.943	-1.310	56.80
6027.051		4.076	-1.210	58.01
6056.005		4.733	-0.460	30.11
6151.617		2.176	-3.299	90.37
6180.203		2.727	-2.780	59.78
6230.722		2.559	-1.281	169.2
6252.555		2.404	-1.687	178.0
6411.648		3.654	-0.820	123.1
6593.870		2.433	-2.422	124.8
5197.577	Fe II	3.231	-2.100	62.05
5234.625		3.221	-2.050	69.02

Table A.10: Element Line-list HE 2144-1832

Wavelength (Å)	Element	E.P. low (eV)	log (gf)	Equivalent width (mÅ)
5682.633	Na I	2.102	-0.700	48.70
5688.205	Na I	2.105	-0.450	85.22
5528.405	Mg I	4.346	-0.620	173.0
6318.717	Mg I	5.108	-1.730	38.08
6783.680	Al I	4.021	-1.440	23.64
5793.073	Si I	4.930	-2.060	86.94
5261.704	Ca I	2.521	-0.730	105.2
5594.462	Ca I	2.523	-0.050	150.4
6449.808	Ca I	2.521	-0.550	131.1
6471.662	Ca I	2.526	-0.590	148.3
6499.650	Ca I	2.523	-0.590	146.1
6245.637	Sc II	1.507	-0.980	96.19
4512.734	Ti I	0.836	-0.480	90.55
4617.269	Ti I	1.789	0.389	77.69
6556.062	Ti I	1.460	-1.074	38.67
4568.314	Ti II	1.224	-2.650	44.15
5185.913	Ti II	1.893	-1.350	98.02
5727.652	V I	1.051	-0.870	29.26
6531.415	V I	1.218	-0.840	21.79
4626.173	Cr I	0.968	-1.320	104.0
5247.565	Cr I	0.961	-1.640	113.2
5348.315	Cr I	1.004	-1.290	115.9
4761.512	Mn I	2.953	-0.138	50.29
4765.846	Mn I	2.941	-0.080	49.18
4766.418	Mn I	2.920	0.100	67.28
4813.467	Co I	3.216	0.050	40.57
4470.472	Ni I	3.399	-0.310	36.00
5035.357	Ni I	3.635	0.290	51.77
5081.107	Ni I	3.847	0.300	47.86
5084.089	Ni I	3.678	0.030	53.99
4810.528	Zn I	4.078	-0.137	51.82

Table A.11: Element Line-list HE 2144-1832 continuing

Wavelength (Å)	Element	E.P. low (eV)	log (gf)	Equivalent width (mÅ)
4607.327	Sr I	0.000	-0.570	53.64
5087.416	Y II	1.084	-0.170	134.2
5289.815	Y II	1.033	-1.850	66.88
5662.925	Y II	1.944	0.160	99.13
4739.480	Zr I	0.651	0.230	82.55
4772.323	Zr I	0.623	0.040	85.68
6134.585	Zr I	0.000	-1.280	67.47
5853.668	Ba II	0.604	-1.000	166.8
4619.874	La II	1.754	-0.140	42.96
4748.726	La II	0.927	-0.860	61.72
4560.280	Ce II	0.910	0.000	50.71
4773.941	Ce II	0.924	-0.498	37.73
5330.556	Ce II	0.869	-0.760	35.85
5322.772	Pr II	0.483	-0.315	85.12
4446.384	Nd II	0.205	-0.590	81.73
4446.384	Nd II	0.205	-0.590	81.73
4451.563	Nd II	0.380	-0.040	106.4
4797.153	Nd II	0.560	-0.950	40.37
4811.342	Nd II	0.064	-1.140	83.63
5089.832	Nd II	0.205	-1.160	73.71
5276.869	Nd II	0.859	-0.440	69.44
5319.815	Nd II	0.550	-0.210	89.75
4499.475	Sm II	0.248	-1.413	54.68
4519.630	Sm II	0.544	-0.751	52.96
4704.400	Sm II	0.000	-1.562	52.43
6437.640	Eu II	1.320	-0.276	25.04